

# Numerical Simulation of Non-premixed Turbulent Combustion Using the Eddy Dissipation Concept and Comparing with the Steady Laminar Flamelet Model

Dmitry A. Lysenko · Ivar S. Ertesvåg ·  
Kjell Erik Rian

Received: 2 January 2014 / Accepted: 3 June 2014 / Published online: 15 June 2014  
© Springer Science+Business Media Dordrecht 2014

**Abstract** Numerical simulations of the Sandia flame CHNa and the Sydney bluff-body stabilized flame HM1E are reported and the results are compared to available experimental data. The numerical method is based on compressible URANS formulations which were implemented recently in the OpenFOAM toolbox. In this study, the calculations are carried out using the conventional compressible URANS approach and a standard  $k$ - $\epsilon$  turbulence model. The Eddy Dissipation Concept with a detailed chemistry approach is used for the turbulence-chemistry interaction. The syngas (CO/H<sub>2</sub>) chemistry diluted by 30 % nitrogen in the Sandia flame CHNa and CH<sub>4</sub>/H<sub>2</sub> combustion in the Sydney flame HM1E are described by the full GRI-3.0 mechanism. A robust implicit Runge-Kutta method (RADAU5) is used for integrating stiff ordinary differential equations to calculate the reaction rates. The radiation is treated by the P1-approximation model. Both target flames are predicted with the Steady Laminar Flamelet model using the commercial code ANSYS FLUENT as well. In general, there is good agreement between present simulations and measurements for both flames, which indicates that the proposed numerical method is suitable for this type of combustion, provides acceptable accuracy and is ready for further combustion application development.

**Keywords** Sandia flame CHNa · Sydney flame HM1E · Compressible  
Reynolds-averaged simulations · RADAU5 · Eddy Dissipation Concept · OpenFOAM

---

D. A. Lysenko (✉) · I. S. Ertesvåg  
Department of Energy and Process Engineering, Norwegian University of Science and Technology,  
Kolbjørn Hejes vei 1B, NO-7491, Trondheim, Norway  
e-mail: dmitry.lysenko@ntnu.no

K. E. Rian  
Computational Industry Technologies AS, NO-7462, Trondheim, Norway

## 1 Introduction

The goal of the present work is detailed validation of the Eddy Dissipation Concept with detailed chemistry which was implemented in the OpenFOAM toolbox. The core numerical method is based on the OpenFOAM toolbox which was originally developed as a high-end C++ classes library (Field Operation and Manipulation) for a broad range of fluid dynamics applications. Today, the OpenFOAM toolbox is very popular in industrial engineering as well as in academic research (for example, there are at least two annual international conferences dedicated to the library development and evaluation). Previously, methodical investigations for several turbulent bluff-body flows have been carried out with the goal of verification, validation and understanding of the capabilities of the numerical method using the conventional approach for solution of the unsteady compressible Reynolds-averaged Navier-Stokes equations (URANS) [31]. These results were analyzed in detail and agreed fairly well with experimental data.

Recently, Lilleberg et al. [29] carried out several turbulent combustion calculations of well-known detailed flame experiments such as the Sandia Flames D, E [2] and a piloted lean-premixed jet burner (PPJB) [10, 11]. Lilleberg and his co-workers [29] used a classical approach for the solution of the steady, compressible Reynolds-averaged Navier-Stokes (RANS) equations, where the turbulence was treated via a standard  $k$ - $\epsilon$  model [27] and several ways of coupling chemical kinetics with the Eddy Dissipation Concept (hereafter EDC) [15] were adopted. As was expected, the detailed chemistry approach showed the best agreement with the measured data for all cases.

In the present study, the solver originally developed by Lilleberg et al. [29] was updated to the unsteady, compressible Reynolds-averaged Navier-Stokes (URANS) equations. The turbulence-chemistry interaction was treated according to the Eddy Dissipation Concept with the detailed chemistry approach. The validation was extended with two benchmark flames: the Sandia flame CHNa [3] and the Sydney bluff-body flame HM1E [9]. The Sandia flame CHNa has the advantage of a simple geometry, which enables modelers to focus on the role of the turbulence and chemical kinetic models in the simulations, and minimizes other factors related to so-called discretization errors [36]. Thus, it was possible to investigate the influence of chemical kinetics, turbulence-chemistry interaction and radiation heat transfer for this flame. Bluff-body stabilized flames are still a challenging case for turbulent combustion modeling due to the complexity of the turbulent flow and finite-rate chemistry, which results in high dimensionality and requires integration of stiff differential equations of chemical kinetics [30].

For the sake of completeness, both flames were also simulated using the Steady Laminar Flamelet (SLF) model. The commercial code ANSYS FLUENT was utilized for this purpose. It is worth noticing that the same grids were used in calculations by OpenFOAM and ANSYS FLUENT. For both codes, numerical methods and boundary conditions were kept as close as possible. Side-by-side comparison of the results obtained by the EDC and SLF models and in experiments is presented and discussed.

The paper is divided into six main parts. The first and the second part of the paper describes the mathematical and numerical modeling, respectively. Then, a general description of the test cases is given. Finally, computational results are presented, analyzed and discussed, and conclusions are drawn.

## 2 Mathematical Modeling

### 2.1 Governing equations

The Favre-averaged (i.e. mass-density-weighted) equations of mass, momentum and energy for turbulent compressible flow are:

$$\frac{\partial \bar{\rho}}{\partial t} + \frac{\partial}{\partial x_j} (\bar{\rho} \tilde{u}_j) = 0, \quad (1)$$

$$\frac{\partial}{\partial t} (\bar{\rho} \tilde{u}_i) + \frac{\partial}{\partial x_j} (\bar{\rho} \tilde{u}_i \tilde{u}_j) = -\frac{\partial \bar{p}}{\partial x_i} + \frac{\partial}{\partial x_j} (\bar{\tau}_{ij} - \bar{\rho} \tilde{u}_i'' \tilde{u}_j''), \quad (2)$$

$$\frac{\partial}{\partial t} (\bar{\rho} \tilde{h}) + \frac{\partial}{\partial x_j} (\bar{\rho} \tilde{h} \tilde{u}_j) = \frac{\partial}{\partial x_j} \left( \bar{\rho} \alpha \frac{\partial \tilde{h}}{\partial x_j} - \bar{\rho} \tilde{u}_j'' \tilde{h}'' \right) - \frac{\partial}{\partial x_j} (\bar{q}_r) + \bar{S}_{hc}. \quad (3)$$

Here, the overbar denotes Reynolds averaging, while the tilde denotes Favre averaging:  $\rho$  denotes the density,  $u$  is the velocity,  $p$  is the pressure,  $h = \sum_s Y_s \int C_{p,s} dT$  is the enthalpy,  $T$  is the temperature,  $Y_s$  is the species mass fraction,  $C_{p,s}$  is the heat capacity for species  $s$  in the mixture,  $\alpha$  is the thermal diffusivity,  $q_r$  represents the radiative heat loss and  $S_{hc}$  represents the source term due to combustion.

Here,  $C_{p,s}$  is calculated as a function of temperature from a set of coefficients taken from NIST-JANAF thermochemical tables [5]. The thermal diffusivity is modeled as

$$\bar{\rho} \alpha = \mu \frac{C_v}{C_{pBar}} \left( 1.32 + 1.77 \frac{R}{C_v} \right), \quad (4)$$

where  $\mu$  is the molecular viscosity (calculated according to the Sutherland law),  $R$  is the gas constant,  $C_v$  represents heat capacity at constant volume.  $C_{pBar}$  is the specific heat averaged over the temperature interval from the reference temperature to the actual mean temperature,

$$C_{pBar} = \frac{\Delta h}{\Delta T}, \quad (5)$$

where  $\Delta T = \tilde{T} - T_{ref}$ ,  $\Delta h = \tilde{h}(T) - \tilde{h}(T_{ref})$ .

$\bar{S}_{hc}$  is modeled according to

$$\bar{S}_{hc} = - \sum_{s=1}^N \frac{\bar{\omega}_s}{M_s} h_{f,s}^\theta, \quad (6)$$

where  $h_{f,s}^\theta$  is the species formation enthalpy,  $M_s$  is the species molecular weight and  $\omega_s$  is the species reaction rate.

The turbulence flux  $\widetilde{u_j'' h''}$  is derived according to the gradient hypothesis

$$-\bar{\rho} \widetilde{u_j'' h''} \approx \frac{\mu_t}{Pr_t} \frac{\partial \tilde{h}}{\partial x_j}, \quad (7)$$

where  $\mu_t$  is the turbulence viscosity and  $Pr_t$  is a turbulence Prandtl number (here  $Pr_t = 0.7$ ).

For a mixture of  $N_s$  species (where  $s = 1 \dots N_s$ ), a transport equation for the mean mass fraction of an individual species  $Y_s$  can be defined according to

$$\frac{\partial}{\partial t} (\bar{\rho} \tilde{Y}_s) + \frac{\partial}{\partial x_j} (\bar{\rho} \tilde{Y}_s \tilde{u}_j) = \frac{\partial}{\partial x_j} \left( \left( \bar{\rho} D_{m,s} + \frac{\mu_t}{Sc_t} \right) \frac{\partial \tilde{Y}_s}{\partial x_j} \right) + \bar{\omega}_s, \quad s = 1, \dots, N_s, \quad (8)$$

where  $D_{m,s}$  is the mass diffusion coefficient for species  $s$  in a mixture,  $Sc_t$  is the turbulence Schmidt number ( $Sc_t = \mu_t / \rho D_t$ , where  $D_t$  is a turbulence diffusivity). Here, Fick's law is introduced and the diffusion coefficient was set equal for all species,  $D_{m,s} = D_m = 2.88 \times 10^{-5} \text{ m}^2/\text{s}$ . The turbulence Schmidt number was set to 0.7. Finally, the temperature is related to the density and the pressure by the ideal gas law.

The stress tensor for a Newtonian fluid is expressed as

$$\bar{\tau}_{ij} = \mu \left( \frac{\partial \tilde{u}_i}{\partial x_j} + \frac{\partial \tilde{u}_j}{\partial x_i} \right) - \frac{2}{3} \mu \delta_{ij} \frac{\partial \tilde{u}_k}{\partial x_k}. \quad (9)$$

The Reynolds stresses are modeled according to

$$\bar{\rho} \widetilde{u_i'' u_j''} = -\mu_t \left( \frac{\partial \tilde{u}_i}{\partial x_j} + \frac{\partial \tilde{u}_j}{\partial x_i} - \frac{2}{3} \delta_{ij} \frac{\partial \tilde{u}_k}{\partial x_k} \right) + \frac{2}{3} \bar{\rho} \tilde{k} \delta_{ij}. \quad (10)$$

The standard  $k$ - $\epsilon$  model [27] is based on the turbulence kinetic energy ( $\tilde{k}$ ) and its dissipation rate ( $\tilde{\epsilon}$ ). The turbulence viscosity is defined here as  $\mu_t = C_\mu \bar{\rho} \tilde{k}^2 / \tilde{\epsilon}$ .

The modeled transport equations are:

$$\frac{\partial}{\partial t} (\bar{\rho} \tilde{k}) + \frac{\partial}{\partial x_j} (\bar{\rho} \tilde{k} \tilde{u}_j) = \frac{\partial}{\partial x_j} \left( \left( \mu + \frac{\mu_t}{\sigma_k} \right) \frac{\partial \tilde{k}}{\partial x_j} \right) + G - \bar{\rho} \tilde{\epsilon}, \quad (11)$$

$$\frac{\partial}{\partial t} (\bar{\rho} \tilde{\epsilon}) + \frac{\partial}{\partial x_j} (\bar{\rho} \tilde{\epsilon} \tilde{u}_j) = \frac{\partial}{\partial x_j} \left( \left( \mu + \frac{\mu_t}{\sigma_\epsilon} \right) \frac{\partial \tilde{\epsilon}}{\partial x_j} \right) + C_{\epsilon 1} \frac{\tilde{\epsilon}}{\tilde{k}} G - C_{\epsilon 2} \bar{\rho} \tilde{\epsilon} \frac{\tilde{\epsilon}^2}{\tilde{k}}, \quad (12)$$

where  $\mu$  is the molecular viscosity, and the rate of turbulence kinetic energy production  $G$  is given as

$$G = -\bar{\rho} \widetilde{u_i'' u_j''} \frac{\partial \tilde{u}_i}{\partial x_j}. \quad (13)$$

The standard values [27] are used for the model constants  $C_\mu$ ,  $C_{\epsilon 1}$ ,  $C_{\epsilon 2}$ ,  $\sigma_k$  and  $\sigma_\epsilon$ .

## 2.2 EDC for turbulent combustion

The Eddy Dissipation Concept for turbulent combustion [15, 33] is based on the energy cascade model [50]. The EDC assumes that molecular mixing and chemical reactions occur in the fine structures of the turbulent flow where the smallest dissipative eddies are present. The characteristic length  $L^*$  and velocity  $u^*$  scales of the fine structures are of the same order of magnitude as the Kolmogorov scales and can be expressed as

$$L^* = \frac{2}{3} \left( \frac{3C_{D2}^3}{C_{D1}^2} \right)^{1/4} \left( \frac{v^3}{\tilde{\epsilon}} \right)^{1/4}, \quad (14)$$

$$u^* = \left( \frac{C_{D2}}{3C_{D1}^2} \right)^{1/4} (v\tilde{\epsilon})^{1/4}, \quad (15)$$

where  $C_{D1} = 0.134$  and  $C_{D2} = 0.5$  [15]. The RANS-based EDC assumes that the full cascade takes place at each numerical cell, and the connection between the fine structure and

the larger eddies is achieved through the cascade. Thus, characteristics of the large eddies such as the velocity  $u'$  are evaluated using the turbulence model (in the present case, the standard  $k - \epsilon$  model).

In the model expressed below, different superscripts refer to states inside the fine structures (\*), the surroundings (o) and the mean values of the computational cell ( $\sim$ ).

In this study, the ratio between the mass in the fine structures and the total mass was taken as

$$\gamma^* = \left( \frac{u^*}{u'} \right)^2 = \left( \frac{3C_{D2}}{4C_{D1}^2} \right)^{1/2} \left( \frac{v\tilde{\epsilon}}{\tilde{k}^2} \right)^{1/2}, \quad (16)$$

as suggested by Magnussen [34].

The mass exchange between the fine structures and the surroundings, divided by the mass of the fine structures, is defined as

$$\dot{m}^* = 2 \frac{u^*}{L^*} = \left( \frac{3}{C_{D2}} \right)^{1/2} \left( \frac{\tilde{\epsilon}}{v} \right)^{1/2}. \quad (17)$$

The mass exchange between the fine structures and the surroundings, divided by the total mass, is calculated according to

$$\dot{m} = \gamma^* \dot{m}^*. \quad (18)$$

The mass-averaged mean reaction rate for the  $s$  specie is given as

$$-\bar{\omega}_s = \frac{\bar{\rho} \dot{m} \zeta}{1 - \gamma^* \zeta} (\tilde{Y}_s - Y_s^*), \quad s = 1, \dots, N_s \quad (19)$$

and the relationship between the mass-averaged mean state, fine-structure state and surrounding state is expressed as

$$\tilde{\Psi} = \gamma^* \zeta \Psi^* + (1 - \gamma^* \zeta) \Psi^o. \quad (20)$$

Here,  $\zeta$  is the reacting fraction of the fine structures, which can depend on the probability of co-existence of the reactants, the degree of heating and reaction limitations. In the present study,  $\zeta = 1$ , as suggested by Gran and Magnussen [17]. The mean mass fraction  $\tilde{Y}_s$  for species  $s$  is calculated from solving the species mass transport equation for each individual species. The fine-structure mass fraction  $Y_s^*$  is computed through the detailed chemistry approach.

The expression of Eq. 16 [34] represents a change compared to former versions of EDC [17, 33], which had  $\gamma^* = (u^*/u)^3$ . In isotropic turbulence, the ratio of Eq. 16 will be proportional to  $\text{Re}_\lambda^{-1}$ , where  $\text{Re}_\lambda$  is the turbulence Reynolds number based on the Taylor microscale. The previously used expression will be proportional to  $\text{Re}_\lambda^{-3/2}$ . The change has an effect in the RHS denominator of Eq. 19 and in Eq. 20. There is, however, no formal effect in the numerator of Eq. 19. Besides this, there is a change in interpretation. The previous model corresponds to a sheet-like turbulence fine structure (Corrsins model), whereas Eq. 16 corresponds to a tube-like structure (Tennekes model), see [15].

### 2.3 EDC detailed chemistry approach

The finite-rate chemical kinetics are taken into account by treating the fine structures as constant pressure and adiabatic homogeneous reactors. Thus, the fine structures mass fractions

values  $Y_s^*$  can be calculated by solving a system of ordinary differential equations (ODE) describing a Perfectly Stirred Reactor (PSR) [17],

$$\frac{dY_s^*}{dt} = \frac{\omega_s^*}{\rho^*} + \frac{1}{\tau^*} (Y_s^\circ - Y_s^*), \quad s = 1, \dots, N_s. \quad (21)$$

The reaction rate  $\omega_s^*$  is evaluated from a chemical kinetics mechanism.  $Y_s^\circ$  is the mass fraction of the inflow stream to the reactor (cf. Eq. 20). In the present study, it is assumed adiabatic and isobaric PSRs. Further, it is assumed that the PSRs are at steady state [17], meaning that the steady-state solution of Eq. 21 is achieved by integrating it in time to steady state.

It is worth noticing that the residence or mixing time scale  $\tau^*$  is evaluated using the molecular viscosity and the dissipation rate

$$\tau^* = \frac{1}{\dot{m}^*}. \quad (22)$$

The chemical kinetic mechanism GRI-3.0 [4] is used for modeling of both test cases. This mechanism has been specially designed for combustion of natural gas with air and contains 325 elementary reactions and 53 species.

Another kinetic model, consisting of 34 elementary reactions and 14 species [14], is also used for syngas combustion (Sandia Flame CHNa). This mechanism has been developed specially for the applications of syngas combustion by Frassoldati, Faravelli and Ranzi [14] and was validated against a set of experimental measurements (including plug flow reactor, PSR, shock tubes and ignition delay times, laminar flame speed, and ignition in a counter-flow flame). We assigned the acronym FFR to this mechanism, which is formed by the first letters of the developer's last names [14] in the spirit of Marzouk and Huckaby [36].

## 2.4 The mixture fraction probability density function model

In the present study the mixture fraction,  $f$  is defined as [55]

$$f = \frac{Z_i - Z_{i,ox}}{Z_{i,fuel} - Z_{i,ox}}, \quad (23)$$

where  $Z_i$  is the elemental mass fraction for element  $i$ . The subscripts ox and fuel denote the value at the oxidizer and fuel stream inlets, respectively. Using the standard assumptions of the equal diffusion coefficients for all species, and assuming that the considered flow is turbulent (where turbulent convection overwhelms molecular diffusion),  $f$  is the elemental mass fraction. Equation 23 is identical for all elements when the diffusion coefficients are equal for all species. In this case the mixture fraction is the elemental mass fraction that originated from the fuel stream [1]. The Favre-mean transport equation for  $\tilde{f}$  and its variance  $\widetilde{f'^2}$  [1, 25] are

$$\frac{\partial}{\partial t} (\bar{\rho} \tilde{f}) + \frac{\partial}{\partial x_j} (\bar{\rho} \tilde{u}_j \tilde{f}) = \frac{\partial}{\partial x_j} \left( \frac{\mu_t}{Sc_t} \frac{\partial \tilde{f}}{\partial x_j} \right), \quad (24)$$

$$\frac{\partial}{\partial t} (\bar{\rho} \widetilde{f'^2}) + \frac{\partial}{\partial x_j} (\bar{\rho} \tilde{u}_j \widetilde{f'^2}) = \frac{\partial}{\partial x_j} \left( \frac{\mu_t}{Sc_t} \frac{\partial \widetilde{f'^2}}{\partial x_j} \right) + C_g \mu_t \left( \frac{\partial \tilde{f}}{\partial x_j} \right)^2 - C_d \bar{\rho} \frac{\tilde{k}}{\tilde{\epsilon}} \widetilde{f'^2}, \quad (25)$$

where  $f'' = f - \tilde{f}$ ,  $Sc_t = 0.85$ ,  $C_g = 2.86$  and  $C_d = 2$ .

In the present study a chemical equilibrium assumption is used, where reactions rates are sufficiently fast for the mixture to be in a state of chemical equilibrium. With this assumption the equilibrium state of density, temperature and composition can be obtained by minimizing the free energy [55].

In AF the mean values of density, temperature and species mass fractions are determined from look-up tables, depending on mean and variance of the mixture fraction and the mean enthalpy

$$\tilde{\phi}_i = \tilde{\phi}_i(\tilde{f}, \widetilde{f'^2}, \tilde{h}). \quad (26)$$

These tabulated values are obtained by a prescribed PDF  $p(f)$  modeled by a  $\beta$  function and a Dirac delta PDF  $\delta(h - \tilde{h})$ . The latter means that enthalpy fluctuations are assumed independent of the amount of heat transferred. The procedure requires solution of the model transport equation for the enthalpy [1, 21]

$$\frac{\partial}{\partial t}(\bar{\rho}\tilde{h}) + \frac{\partial}{\partial x_j}(\bar{\rho}\tilde{u}_j\tilde{h}) = \frac{\partial}{\partial x_j}\left(\frac{\mu_t}{Pr_t}\frac{\partial \tilde{h}}{\partial x_j}\right) - \frac{\partial}{\partial x_j}(\bar{q}_r), \quad (27)$$

where the AF default value of the turbulence Prandtl number was used,  $Pr_t = 0.7$ .

## 2.5 The steady laminar flamelet (SLF) model

The laminar flamelet model represents the turbulent flame as an ensemble of thin, laminar, locally one-dimensional flamelet structures embedded within the turbulent flow field [43]. In this case the chemical time and length scales need not be resolved and the flame could be described by the mixture fraction and the strain rate (or the scalar dissipation,  $\chi$ ).

The instantaneous scalar dissipation is defined as

$$\chi = 2D_f \left| \frac{\partial f}{\partial x_j} \right|^2, \quad (28)$$

where  $D_f$  is a diffusion coefficient  $\rho D_f = \alpha/C_p$ .

It is assumed that the mixture fraction  $f$  to be given in the flow field as a function of space and time. The surface of stoichiometric mixture can be determined from [43]

$$f(x, y, z, t) = f_{st}. \quad (29)$$

The concept of a laminar diffusion flamelets in a turbulent diffusion flame has been introduced by Williams [58]. Combustion takes place in a thin layer in the vicinity of this surface if the local mixture fraction gradient is sufficiently high. This thin layer and the surrounding inert mixing region is called a laminar diffusion flamelet [43].

The flamelet equations for the species mass fractions and temperature can be derived by application of a universal coordinate transformation and subsequent asymptotic approximation (where the scalars  $T$  and  $Y_s$  are expressed as functions of the the mixture fraction  $f$ ) [43]

$$\rho \frac{\partial Y_s}{\partial t} = \frac{1}{2} \rho \chi \frac{\partial^2 Y_s}{\partial f^2} + \omega_s, \quad (30)$$

$$\rho \frac{\partial T}{\partial t} = \frac{1}{2} \rho \chi \frac{\partial^2 T}{\partial f^2} + \frac{1}{C_p} \frac{\partial p}{\partial t} - \sum_{s=1}^N \frac{1}{C_p} h_s \omega_s. \quad (31)$$

Equations 30–31 rely on the Shvab-Zeldovich formulation of the species mass fraction and energy equations, which involves the approximation of unity Lewis numbers for all species [44].

The flamelet strain rate  $\alpha_S$  can be related to  $\chi$  if  $f$  is not small as [43]

$$\chi = \frac{\alpha_S}{\pi} \exp\left(-2\left(\operatorname{erfc}^{-1}(2f)\right)^2\right), \quad (32)$$

where  $\text{erfc}^{-1}$  represents the inverse complementary error function.

Flamelets are generated at scalar dissipation values as

$$\chi_i = \begin{cases} 10\chi_{i-1} & \text{for } \chi_{i-1} < 1 \text{ s}^{-1} \\ \chi_{i-1} + \Delta\chi & \text{for } \chi_{i-1} \geq 1 \text{ s}^{-1} \end{cases}, \quad (33)$$

where  $i$  ranges from 1 to the specified number of flamelets,  $\chi_0$  is the initial scalar dissipation, and  $\Delta\chi$  is the scalar dissipation step. Here,  $i = 1 \dots 25$ ,  $\chi_0 = 0.01 \text{ s}^{-1}$  and  $\Delta\chi = 5 \text{ s}^{-1}$ . The finite-rate chemistry effects are taken into account by treatment of the FFR and the GRI3.0 mechanisms for the Sandia flame CHNa and the Sydney Flame HM1E, respectively.

The Favre-average of a scalar  $\phi$  can be defined from the PDF of  $f$  and  $\chi$  as

$$\tilde{\phi} = \int \int \phi p(f, \chi) df d\chi, \quad (34)$$

where  $\phi$  represents species mass fraction and temperature.

Using Bayes' theorem the joint PDF of  $f$  and  $\chi$  can be written [43]

$$\tilde{p}(f, \chi) = \tilde{p}_f(f) \tilde{p}_\chi(\chi|f), \quad (35)$$

where  $\tilde{p}_f(f)$  is the marginal distribution

$$\tilde{p}_f(f) = \int_0^\infty \tilde{p}_{f\chi}(f, \chi) d\chi \quad (36)$$

and  $\tilde{p}_\chi(\chi|f)$  is the conditioned PDF of  $\chi$  for a fixed value of  $f$ . Here, the PDF's are specified by tilde as Favre-probability-density functions. Furthermore,  $f$  and  $\chi$  are assumed to be statistically independent [1, 43] so the joint PDF  $\tilde{p}(f, \chi)$  can be simplified as

$$\tilde{p}(f, \chi) = \tilde{p}_f(f) \tilde{p}_\chi(\chi), \quad (37)$$

where

$$\tilde{p}_\chi(\chi) = \int_0^1 \tilde{p}_{f\chi}(f, \chi) df \quad (38)$$

is the marginal distribution.

Equations 24–25 are solved to specify  $p_f$  which is supposed to have the  $\beta$ -PDF shape. The PDF of  $\chi$  is the Delta function assuming that fluctuations are neglected.

The mean scalar dissipation,  $\tilde{\chi}$ , is modeled as [1, 43]

$$\tilde{\chi} = C_\chi \frac{\tilde{\epsilon} \tilde{f}''^2}{\tilde{k}}, \quad (39)$$

where  $C_\chi$  is a constant ( $C_\chi = 2$ ), which may be expected to be valid in the fully turbulent part of shear flows.

For non-adiabatic steady state flamelets it is assumed that heat sources have a negligible effect on the species mass fractions.

## 2.6 Modeling radiation

The radiation is modeled by the P1-approximation, which is the simplest form of the more generalized P-N method (or spherical harmonics) [6] assuming that a flame is optically thin. The radiative heat loss  $\tilde{q}_r$  is calculated as

$$-\frac{\partial}{\partial x_j} \tilde{q}_r = \alpha_c G - 4e_c \sigma T^4, \quad (40)$$



where  $\alpha_c$  is the absorption coefficient ( $\text{m}^{-1}$ ),  $e_c$  is the emission coefficient ( $\text{m}^{-1}$ ) and  $\sigma$  is the Stefan-Boltzmann constant. The incident radiation  $G$  is modeled according to

$$\frac{\partial}{\partial x_j} \left( \Gamma \frac{\partial}{\partial x_j} G \right) - \alpha_c G + 4e_c \sigma T^4 = 0, \quad (41)$$

$$\Gamma = \frac{1}{3(\alpha_c + \sigma_s)}, \quad (42)$$

where  $\sigma_s$  is the scattering coefficient ( $\sigma_s = 1 \text{ m}^{-1}$ ). The absorption coefficient and the emission coefficient are calculated using a weighted-sum-of-gray-gases model (WSGGM) [22] as a function of local concentrations of  $\text{CO}_2$  and  $\text{H}_2\text{O}$ , path-length and pressure. The emissivity weighting factors for  $\text{CO}_2$  and  $\text{H}_2\text{O}$  are taken from Smith et al. [54].

### 3 Brief Description of the Numerical Methodology

A main purpose of this work was to validate the Eddy Dissipation Concept implemented in the OpenFOAM (hereafter OF) toolbox [57]. However, to investigate the influence of the turbulence-combustion interaction modeling, the assumed  $\beta$ -PDF approach and the steady laminar flamelet model (SLF hereafter) were tested as well, using the ANSYS FLUENT (hereafter AF) technology [1].

The standard  $k$ - $\epsilon$  model [27] with wall functions (hereafter SKE) was used to close the Navier-Stokes equations. The  $k$ - $\omega$  Shear Stress Transport (hereafter SST) turbulence model [39, 40] was applied for the Sydney flame HM1E to advance modeling of this separated bluff-body flow. However, a critical remark should be done here due to different implementations of the  $k$ - $\omega$  SST model in OF and AF. The high-Reynolds-number formulation of the  $k$ - $\omega$  SST [40] is implemented in OF assuming that the wall functions are specified for  $\omega$ . In this case one should not expect superior results in predictions over the standard  $k$ - $\epsilon$  model (see Section 5.3). Both, the low-Reynolds-number and the high-Reynolds number formulations are available in AF through the enhanced wall treatment [1]. In the present study, the low-Reynolds-number SST model was assumed for the AF runs.

It is worth noticing that the same grids were used for both solvers.

#### 3.1 OpenFOAM

The new solver was implemented by modification of the build-in OpenFOAM [57] application rhoPisoFoam for the compressible URANS modeling based on the finite-volume method (FVM) [16] and the PISO (pressure implicit with splitting of operators) algorithm [24]. The conjugate gradient method [19] with incomplete Cholesky decompositions of Meijerink and van der Vorst [37] was used for solving the system of linear algebraic equations with a local accuracy of  $10^{-9}$  for all dependent variables at each time step. The numerical method had a second-order accuracy in space and time. The linear-upwind interpolation scheme (the second-order upwind scheme [56]), was applied for all convective terms approximations. A second-order central differences approximation was used to calculate the diffusion terms. A second-order implicit Euler method (BDF-2 [16]) was used for the time integration together with a dynamic adjustable time stepping technique to guarantee a local Courant number less than 0.4.

The calculation of the mean species reaction rate  $\bar{\omega}_s$  requires the integration of Eq. 21 for each computational cell in the domain. For this purpose, the robust RADAU5 algorithm [18]

was used. The RADAU5 algorithm is designed for solving stiff ODE systems and applies a 5th-order accurate implicit Runge-Kutta method based on the Radau quadrature formula. The relative tolerance, absolute tolerance and maximum number of iterations to meet the target accuracy were set to  $5 \times 10^{-5}$ ,  $1 \times 10^{-5}$  and  $10^7$ , respectively.

### 3.2 ANSYS FLUENT

Using the factorized FVM [1] the URANS equations were solved with second-order accuracy in space and time. The velocity and pressure fields were matched with a centered computational template based on the SIMPLEC algorithm [60] and Rhie and Chou filtering [51]. The convective terms were represented according to the Leonard quadratic upwind scheme (QUICK) [28, 56]. The linear system of equations was solved with the Gauss-Seidel iterations or the incomplete lower upper (ILU) decomposition smoothers, which were accelerated by an algebraic multi-grid (AMG) technique, based on the additive-correction strategy [23]. A second-order implicit dual-step method was used for time integration with a constant time step of  $10^{-5}$  s.

## 4 Description of Test Cases

### 4.1 Sandia Flame CHNa

The turbulent non-premixed syngas 40 %CO/30 %H<sub>2</sub>/30 %N<sub>2</sub> (by volume) flame investigated experimentally by Sandia National Laboratories (scalar measurements) and the Swiss Federal Institute of Technology (LDA measurements) [3] was examined. The burner tube had an inner diameter  $D = 4.58 \times 10^{-3}$  m and an outer diameter of  $6.34 \times 10^{-3}$  m. The tube had a thickness of only  $0.88 \times 10^{-3}$  m. However, this was sufficient for flame stabilization via a small recirculation zone. The fuel jet Reynolds number was  $Re_j = U_j D / \nu_j = 16.7 \times 10^3$ , where  $U_j = 76$  m/s was the fuel jet velocity and  $\nu_j = 2.083 \times 10^{-5}$  m<sup>2</sup>/s was the kinematic viscosity. The jet temperature was 292 K. The co-flow stream had a velocity of 0.7 m/s, a temperature of 290 K and a 1.2 % mole fraction of water vapor. Experimental data include axial and radial profiles of mean and root-mean-square (rms) values of temperatures and major species mass fractions as well as velocities and Reynolds stresses.

Some details of the grid and computational domain are shown in Fig. 1. The axial and radial dimensions of the computational domain after the burner exit were set to 0.6 m ( $131 \times D$ ) and 0.2 m ( $43.627 \times D$ ), respectively. The number of computational cells along the axial direction was 230 and the number of cells in the radial direction was 100. The length of the pre-inlet fuel pipe was 0.05 m ( $10.917 \times D$ ) and contained 90 cells. The grid expansion factors were 1.09 and 1.14 in the axial and radial directions (from the burner tube), respectively. There were 10 cells along the inner radius of the fuel jet and 4 cells along the burner tube wall with uniform distribution in the radial direction.

Several studies of the CHNa flame are available in the literature. Cuoci et al. [8] have modeled numerically the CHNa and CHNb flames using RANS with several different turbulence-chemistry interaction approaches, such as the Eddy Dissipation Concept [15, 32] and the steady laminar flamelets model [12]. They reported that the EDC (coupled with the FFR kinetic mechanism) provided the best results.

In contrast to Cuoci et al. [8], Marzouk and Huckaby [36] have studied the CHNa flame using the URANS approach and adopted Chalmers' partially stirred reactor model (PASR) [52] for the turbulence-chemistry interaction and investigated eight chemical kinetic

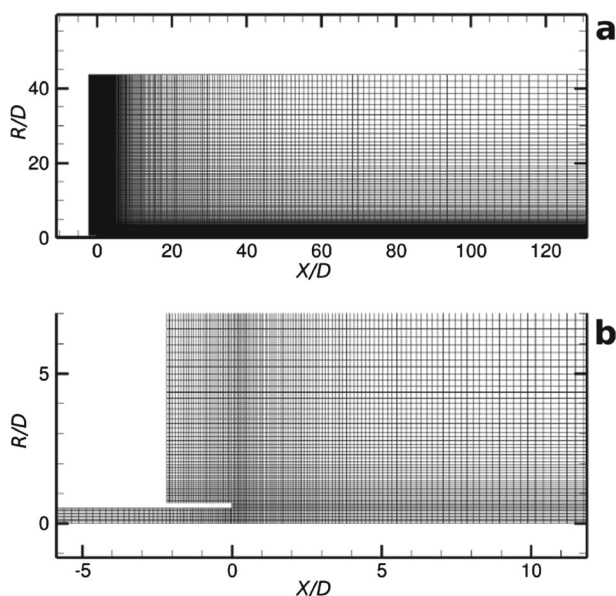


**Fig. 1** A general view of the computational domain (a) and details of the grid near the inlet (b) for the Sandia CHNa flame.  $X$  and  $R$  are the domain coordinates in the axial and radial direction, respectively

mechanisms (including the FFR model). However, Marzouk and Huckaby obtained the most accurate predictions with a simple 3-step/5-species kinetic model.

#### 4.2 Sydney bluff-body flame HM1E

The Sydney bluff-body Flame HM1E configuration consisted of a rotationally symmetric bluff-body nozzle (with the diameter  $D_B = 0.05$  m and the radius  $R_B = D_B/2$ ) which was placed in a square duct of 0.13 m width. Gas was fed through a centered pipe (diameter of  $3.6 \times 10^{-3}$  m) at a bulk jet velocity of  $U_j = 108$  m/s at ambient conditions with the jet Reynolds number,  $Re_j = 15.8 \times 10^3$ . The fuel in this flame was a mixture of hydrogen ( $H_2$ ) and natural gas in the volume ratio 1 : 1. The secondary air stream between the duct and the burner nozzle was fixed at 35 m/s. All velocities and velocity fluctuations were measured by Laser Doppler Velocimetry (LDV), and scalar measurements were carried out using the Raman/Rayleigh/LIF techniques [9].

Some details of the grid and computational domain are shown in Fig. 2. The axial and radial dimensions of the computational domain after the bluff-body were set to 0.5 m ( $20 \times D_B$ ) and 0.15 m ( $6 \times D_B$ ), respectively. The number of cells along the axial direction was 170, and the number of cells in the radial direction was 120. The grid expansion factors were 1.1 and 1.12 in the axial and radial directions (from the bluff-body), respectively. The length of the pre-inlets for the fuel pipe and co-flow was 0.05 m ( $2 \times D_B$ ) and contained 50 cells. The number of computational cells (in the radial direction) located in the jet, bluff-body and co-flow was 8, 60 and 52, respectively. The inner radius of the fuel jet had a uniform distribution of cells in the radial direction, while the bluff-body had bi-exponentiation distribution of nodes from the mid to the fuel jet and co-flow.

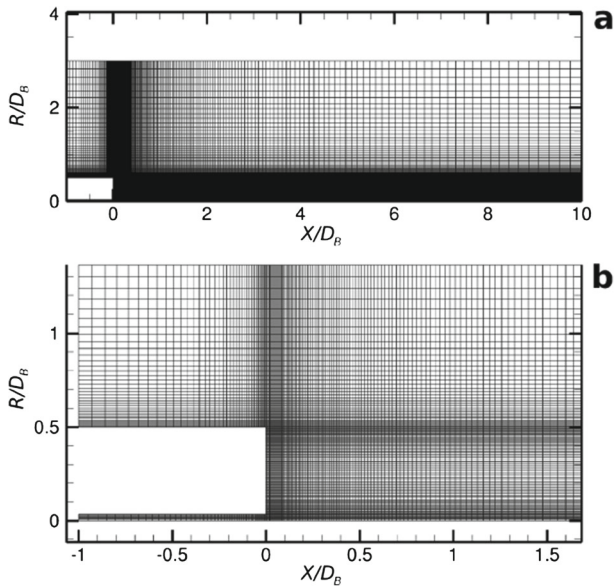


**Fig. 2** General view of the computational domain (a) and details of the grid near the inlet (b) for the Sydney bluff-body HM1E flame.  $X$  and  $R$  are the domain coordinates in the axial and radial direction, respectively

Several researchers have performed simulations of the Sydney bluff-body flames with different turbulence and combustion models. Liu et al. [30] provides a comprehensive overview of previous work. However, it is worth noticing that there is a lack of published data related to the use of the EDC coupled with the detailed chemistry approach.

#### 4.3 Boundary conditions

All problems were solved assuming symmetry about the centerline. For all cases, a computational domain was designed as a sector of  $5^\circ$  with imposed periodic boundary conditions and included pre-inlet pipes for the fuel jet in order to obtain fully-developed turbulent velocity profiles. Uniform velocity profiles were specified for jet and co-flow streams. All radial and circumferential velocity components were set to be zero. The inflow temperatures were specified based on the experimental settings. A zero gradient pressure boundary was applied for all inflow boundaries, while the exit pressure was specified to  $10^5$  Pa at the outlet. A non-slipping condition for velocity was applied to the walls. The temperature at the walls was fixed (iso-thermal) and set according to the experimental data. Wall-functions were applied for  $\tilde{k}$ ,  $\tilde{\epsilon}$  and  $\tilde{\omega}$  (for OF). The enhanced wall treatment was used for  $\tilde{\omega}$  for AF. The inlet values for  $\tilde{k}$  and  $\tilde{\epsilon}$  ( $\tilde{\omega}$ ) were calculated for a turbulence intensity of 5 %, and the turbulence length scale estimated as 7 % of the inlet diameters. The fuel jet, pilot and co-flow compositions were specified in terms of the species mass fractions calculated from the experimental data. Zero-gradient diffusion boundary conditions were applied for species at the walls. Marshak's boundary conditions, based on solutions of Legendre polynomials of odd order [35], were adopted for radiative heat flux calculations.

#### 4.4 Grid dependence study

The present EDC-based results (calculated by OF) were obtained using two sets of grids for each of the flames: a low-resolution grid and a high resolution grid. The high-resolution grids were created by simple refinement of the low-resolution grids by a factor of  $2 \times 2$  in the axial and radial directions. The details of the high-resolution grids are provided in the Sections 4.1 and 4.2. In general, the differences between the two sets of grids were insignificant for the mean velocities, temperature and main species such as  $O_2$ ,  $N_2$ ,  $CO_2$ ,  $H_2O$  and  $H_2$ . However, for the intermediate species such as  $CO$ ,  $OH$  and  $NO$ , high-resolution grids provide more accurate results. Therefore, the EDC-based and the PDF-based results discussed below were obtained using the high-resolution grids. Further grid refinement was not carried out due to resource limitations.

### 5 Results

#### 5.1 Present predictions

All simulated cases are listed in Table 1 (where the following abbreviations are used: F – flame CHNa or HM1E, C – code OF or AF, TM – turbulence model, TCM – turbulence-chemistry interaction model, CH – chemistry mechanism and R – radiation model).

For a quantitative validation of the present simulations the averages have been obtained from the computational results by sampling over four flow-through times, where the flow-through time is defined as the ratio between the axial length of the computational domain to the jet bulk velocity. Hereafter, the time-averaging operator is denoted by  $\langle \rangle$ . The tilde mark denoting Favre-averaging is omitted for the simplicity.

#### 5.2 Sandia Flame CHNa

Figure 3a qualitatively compares the mean axial velocities and the mean temperature along the central axis obtained by OF with the EDC model (run EDC-FFR) with the results by Marzouk and Huckaby [36], who used the Chalmers' PASR model [7, 52] with the FFR

**Table 1** Run matrix

Run	C	F	TM	TCM	CH	R
EDC-FFR	OF	CHNa	SKE	EDC	FFR	P1
EDC-GRI3	OF	CHNa	SKE	EDC	GRI3.0	P1
EDC-GRI3-noRad	OF	CHNa	SKE	EDC	GRI3.0	–
$\beta$ -PDF	AF	CHNa	SKE	$\beta$ -PDF	–	P1
$\beta$ -PDF- $C_{\epsilon 1} = 1.52$	AF	CHNa	SKE ( $C_{\epsilon 1} = 1.52$ )	$\beta$ -PDF	–	P1
$\beta$ -PDF- $C_{\epsilon 1} = 1.60$	AF	CHNa	SKE ( $C_{\epsilon 1} = 1.60$ )	$\beta$ -PDF	–	P1
SLF-FFR- $C_{\epsilon 1} = 1.52$	AF	CHNa	SKE ( $C_{\epsilon 1} = 1.52$ )	SLF	FFR	P1
EDC-GRI3-SKE	OF	HM1E	SKE	EDC	GRI3.0	P1
EDC-GRI3-SST	OF	HM1E	SST	EDC	GRI3.0	P1
SLF-GRI3-SST	AF	HM1E	SST	SLF	GRI3.0	P1
SLF-GRI3-SST- $Sc_t = 0.4$	AF	HM1E	SST	SLF ( $Sc_t = 0.4$ )	GRI3.0	P1

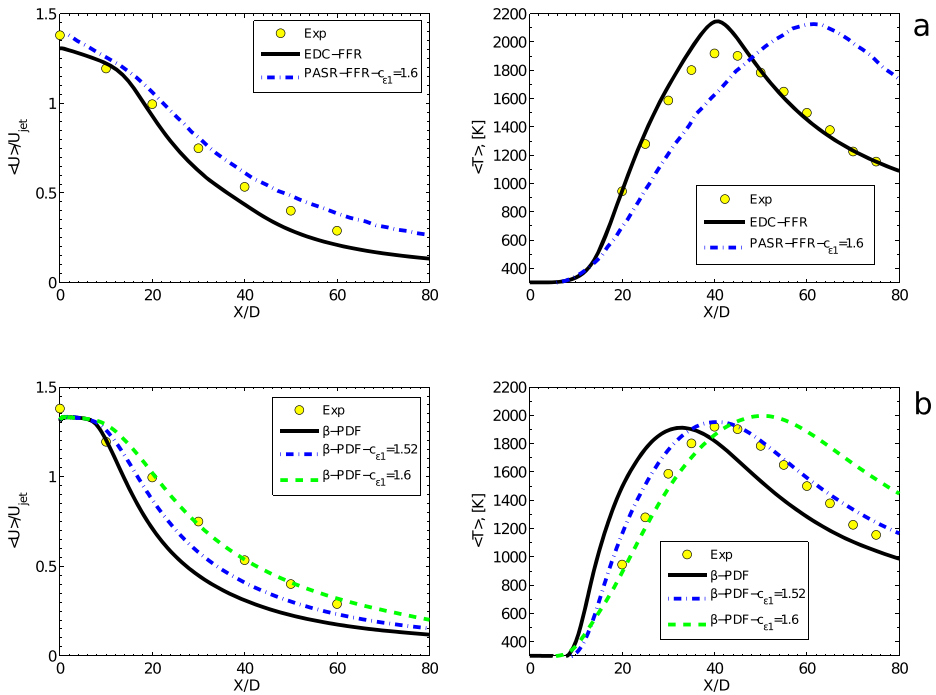


**Fig. 3** Comparison of the predictions by the *EDC* – *FFR* and the *PASR* – *FFR* (extracted from [36]) models of the Sandia Flame CHNa (a). Effect of the  $C_{\epsilon 1}$  constant in the standard  $k$  –  $\epsilon$  model on the Sandia flame CHNa predictions using the assumed  $\beta$  – *PDF* approach (b)

mechanism. Both results were obtained using OF. However, a remark is necessary, since Marzouk and Huckaby [36] applied the standard  $k$  –  $\epsilon$  model with a modified constant  $C_{\epsilon 1} = 1.6$ . On the one hand, one can clearly see that the predictions with the modified constant  $C_{\epsilon 1} = 1.6$  led to the more accurate behavior of the jet penetration. On the other hand, the axial distribution of the flame temperature was significantly shifted downstream and over-estimated in the post-flame zone.

The same observation was found by Cuici et al. [8] in their results obtained by the steady laminar flamelet model [45] coupled with SKE and  $C_{\epsilon 1} = 1.6$ . Further, several additional runs were performed to investigate the effect of the constant  $C_{\epsilon 1}$  using AF with the  $\beta$  – *PDF* approach. Figure 4b shows the predicted mean axial velocities and the mean temperature along the central axis using SKE with  $C_{\epsilon 1} = 1.44$ ,  $C_{\epsilon 1} = 1.52$  and  $C_{\epsilon 1} = 1.6$ , respectively. It could be observed that the higher values of  $C_{\epsilon 1}$  compared to the baseline value of 1.44 led to a more accurate prediction of the mean axial velocity distributions. The present results showed that while the location of the peak temperature is shifted downstream with an increased value of  $C_{\epsilon 1}$ , the post-flame zone became over-estimated. Thus, the compromise value  $C_{\epsilon 1} = 1.52$  may probably be the best choice for the prediction of the Sandia flame CHNa using AF with the assumed  $\beta$  – *PDF* approach.

Figure 4 compares the profiles of the mean temperature and species mass fractions with the experimental data along the central axis for the several runs. In general, the match between numerical and measured results was satisfactory. One can observe some discrepancies for the peak temperatures between the measured and calculated results. A comparison of the predicted flame temperatures is also displayed in Fig. 5. The maximum

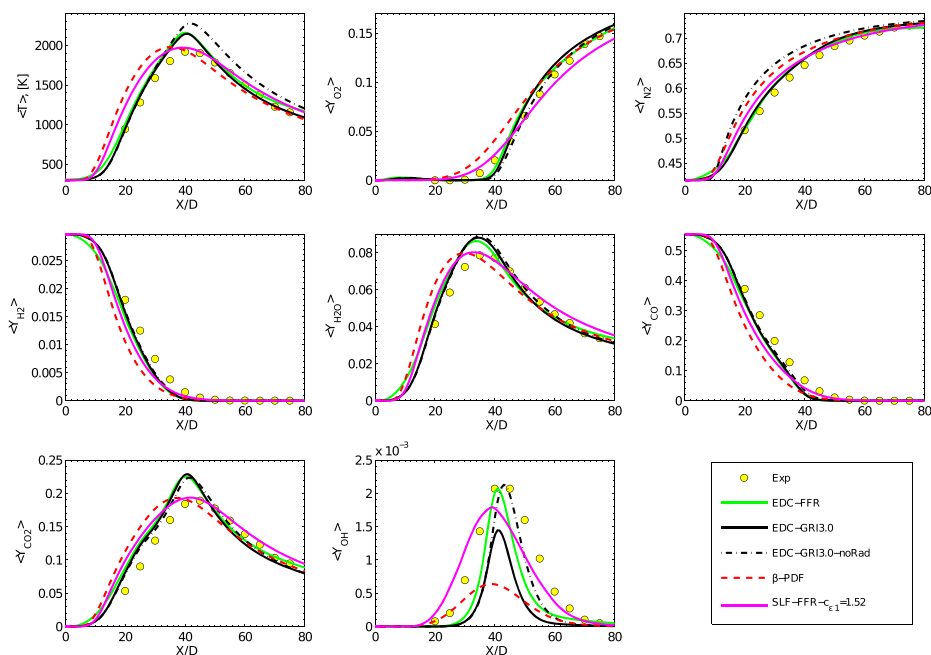


**Fig. 4** Mean temperature and mean composition profiles along the axis for the Sandia flame CHN4

peak temperature ( $\langle T_p \rangle = 2276$  K) was obtained by the EDC run with the GRI3.0 chemistry where no radiation heat transfer was considered. The lowest peak flame temperature was obtained in the measurements ( $\langle T_p \rangle = 1919$  K). The closest to the experimental values  $\langle T_p \rangle = 1978$  K and  $\langle T_p \rangle = 1971$  K were predicted by the  $\beta$ -PDF approach and the SLF model, respectively. The other two runs with the EDC, the P-1 radiation and the FFR and the GRI3.0 chemistry revealed approximately the same peak values  $\langle T_p \rangle = 2160$  K and  $\langle T_p \rangle = 2146$  K, respectively.

Another interesting observation following from Figs. 4 and 5 was the different location of peak temperatures predicted by the applied combustion models. The location of  $\langle T_p \rangle$  obtained by the assumed  $\beta$ -PDF approach was slightly shifted upstream ( $\approx 6X/D$ ) compared to the experimental data, while the EDC-based models predicted the location of  $\langle T_p \rangle$  correctly. The SLF model with the corrected constant  $C_{\epsilon_1} = 1.52$  predicted the peak temperature location quite well.

It is evident as well, that any model overestimation of the flame temperature affect the prediction of the species. The EDC-based models over-estimated the peak temperature by approximately 250 K, hence releasing more thermal energy and producing too high  $\langle Y_{H_2O} \rangle$  and  $\langle Y_{CO_2} \rangle$ . However, all other species such as  $\langle Y_{N_2} \rangle$ ,  $\langle Y_{O_2} \rangle$ ,  $\langle Y_{H_2} \rangle$  and  $\langle Y_{CO} \rangle$  matched well the experimental results. It is worth noticing that only the EDC with the FFR scheme was able to reproduce correctly the behavior of  $\langle Y_{OH} \rangle$ .

An over-prediction of flame temperature may have several reasons. According to Hewson and Kerstein [20], neglecting the radiative heat losses and under-predicting the dissipation rate could be responsible for temperature over-predictions (59 – 241 K). Cuoci et al. [8] reported that thermal radiation affects the peak temperature only by about 30 – 40 K. However, the present results indicated a more significant impact of the thermal radiation on the solution (about 130 K) which could be a consequence of the simple P-1 approach.



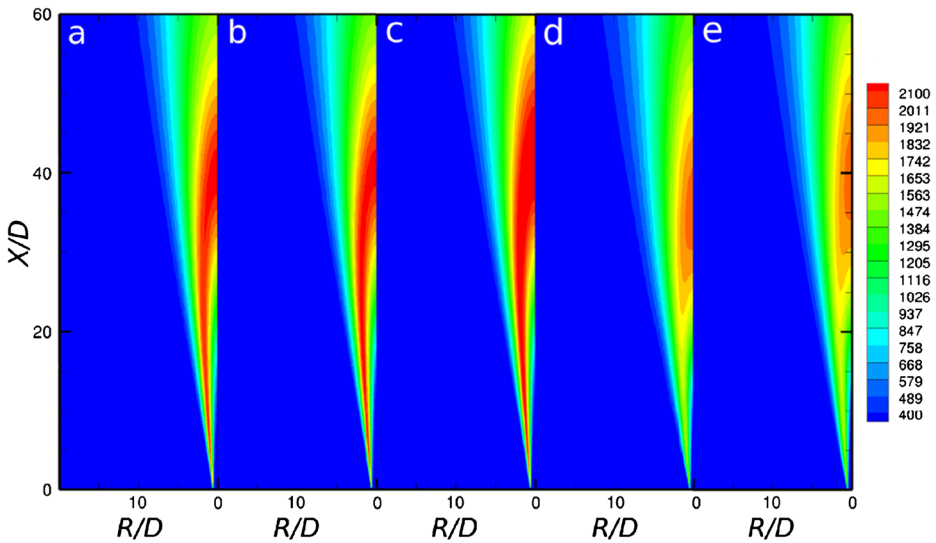


**Fig. 5** Iso-contours of mean temperature for the Sandia flame CHNa: EDC-FFR (a), EDC-GRI3 (b), EDC-GRI3-noRad (c),  $\beta$ -PDF (d) and SLF-FFR- $C_{\epsilon 1} = 1.52$  (e)

Furthermore, Cuoci et al. [8] investigated in detail the effect of the grid density and the applied numerical schemes and concluded that the peak temperature was nearly insensitive to these factors. Cuoci et al. [8] suggested that the most important factor was the turbulence model used. Indeed, different turbulence models affect the jet penetration and the scalar dissipation rate and turbulent mixing.

Furthermore, it is interesting to compare the predicted mean axial velocities with the experimental data (Fig. 6). It is observed that the present results under-estimated to some extent the jet velocity down-stream the central axis. The divergence between predictions by SLF and EDC was not significant. The discrepancies between the SLF model and the measured data could possibly be explained by compressibility effects. Hewson and Kerstein [20] carried out a detailed investigation of such phenomena and suggested that the dilatation of the flow was a possible explanation for these discrepancies. According to Hewson and Kerstein [20] dilatation pushes the fluid downstream leading to higher mixture fractions on the axis and affecting the dissipation rate. Subsequently, increased dissipation rates cause

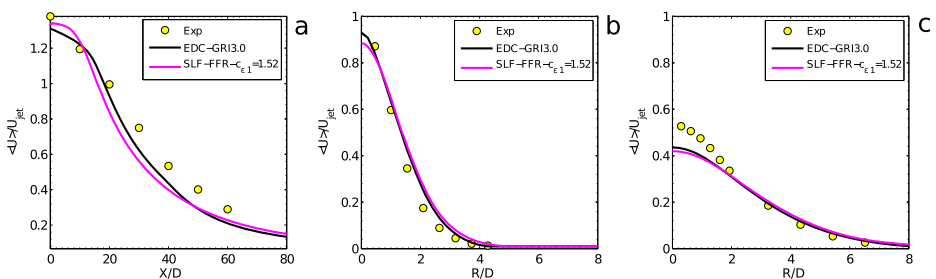


**Fig. 6** Mean axial velocity along the axis (a) and at axial positions  $X/D = 20$  (b) and  $X/D = 40$  (c) for the Sandia flame CHNa



more rapid mixing and a greater rate of decay of the axis mixture fraction. The radial profiles of the mean axial velocities at the axial distances  $X/D = 20$  and  $X/D = 40$  further mimicked the behavior of the axial distributions. At  $X/D = 20$  the predicted jet spreading matched well the measured data when using OF with the EDC approach and AF with the SLF model. Based on the comparison of the predicted and measured radial profiles of the mean axial velocity at  $X/D = 40$  downstream the nozzle exit, it was evident that both OF with the EDC and AF with the SLF model significantly over-estimated the decay of the jet by  $\sim 15\%$ .

A detailed comparison of the radial profiles of the mean temperature and the mean composition at the axial distances  $X/D = 20$  and  $X/D = 40$  is presented in Figs. 7 and 8, respectively. In general, the agreement between the predicted and the measured data was reasonable. The existing discrepancies may be explained by the behavior of the predicted velocity field, e.g. jet penetration and spreading/diffusion.

Figure 9 shows scatter plots of the temperature as a function of mixture fraction by the experiment and the SLF model at the axial distances  $X/D = 20$  and  $X/D = 40$ . The experimental conditional mean of the temperature is shown in Fig. 9 as well. Overall, the agreement between calculations and the experiment was good. One can observe that the maximum temperature at both locations was slightly over-predicted. The match between the predicted and conditional mean temperatures was good up to  $\langle f \rangle = 0.6$  and  $\langle f \rangle = 0.26$  at  $X/D = 20$  and  $X/D = 40$ , respectively.

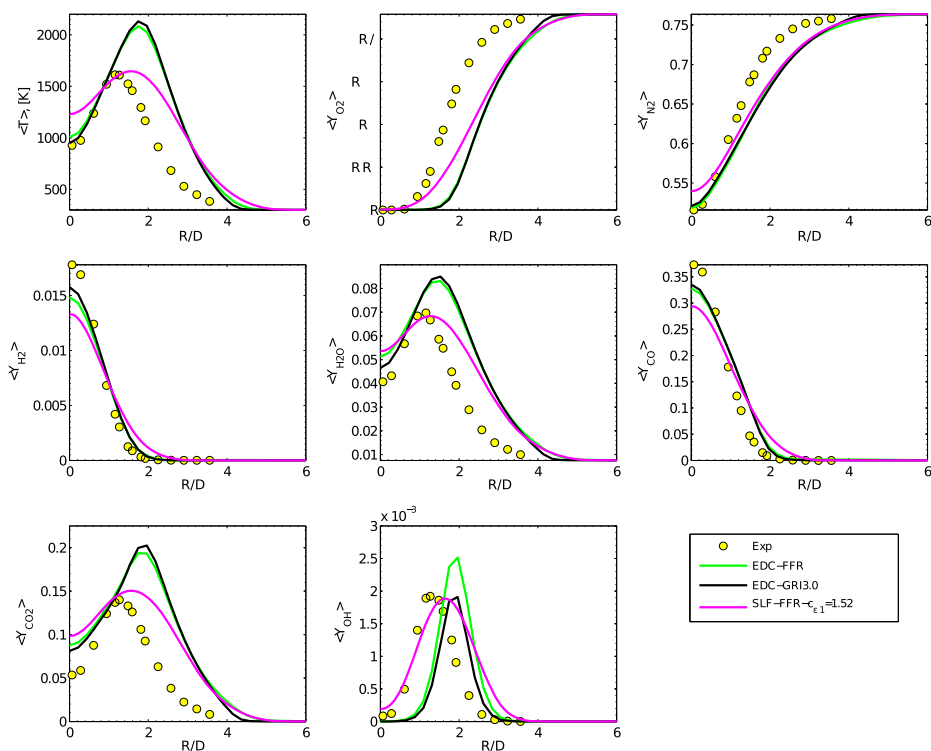


**Fig. 7** Mean temperature and mean composition radial profiles at  $X/D = 20$  for the Sandia flame CHNa

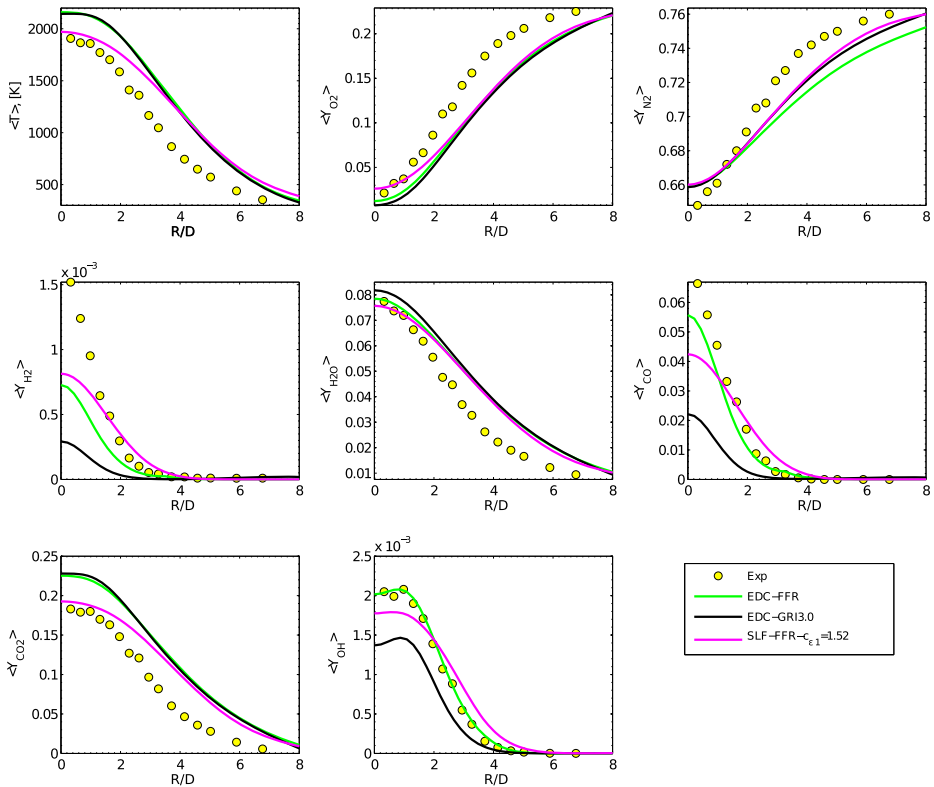


**Fig. 8** Mean temperature and mean composition radial profiles at  $X/D = 40$  for the Sandia flame CHNa

In general, the predicted results by OF with the EDC-based approach and AF with the SLF model (and corrected  $C_{\epsilon 1}$  constant) matched well the experimental data. On the one

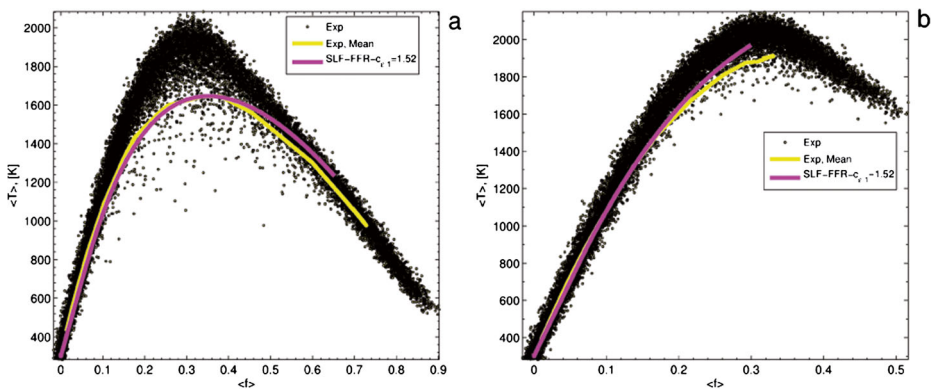


**Fig. 9** Scatterplots of temperature against mixture fraction for the Sandia flame CHNa at  $X/D = 20$  (a) and  $X/D = 40$  (b)

hand, the deviations related with the EDC-based approach could be explained as a consequence of using a not corrected  $k-\epsilon$  model. On the other hand, the effect of dilatation could be considered as the most important for the SLF model (and the  $\beta$ -PDF approach).

### 5.3 Sydney bluff-body flame HM1E

Predicted radial profiles of the mean velocities for the Sydney flame HM1E were compared to experimental data in Fig. 10. Overall, the agreement between the present data and the measurements was good at upstream locations within the recirculation zone. Both the shape and the peak values of the radial profiles of the mean axial ( $U$ ) and radial ( $V$ ) velocities were well captured in this region. The jet penetration depth, the spreading and the positions of the two shear layers were predicted quite well. It is interesting to note that the axial velocities predicted by OF with the SKE and SST turbulence models decayed too quickly at the symmetry axis compared to the experimental data. This was in agreement with the predictions by Yan et al. [59] and Liu et al. [30]. In spite of that the magnitudes of mean radial velocities were significantly smaller than the magnitudes of the mean axial velocities (approximately by one order of magnitude), the agreement between them was reasonable.

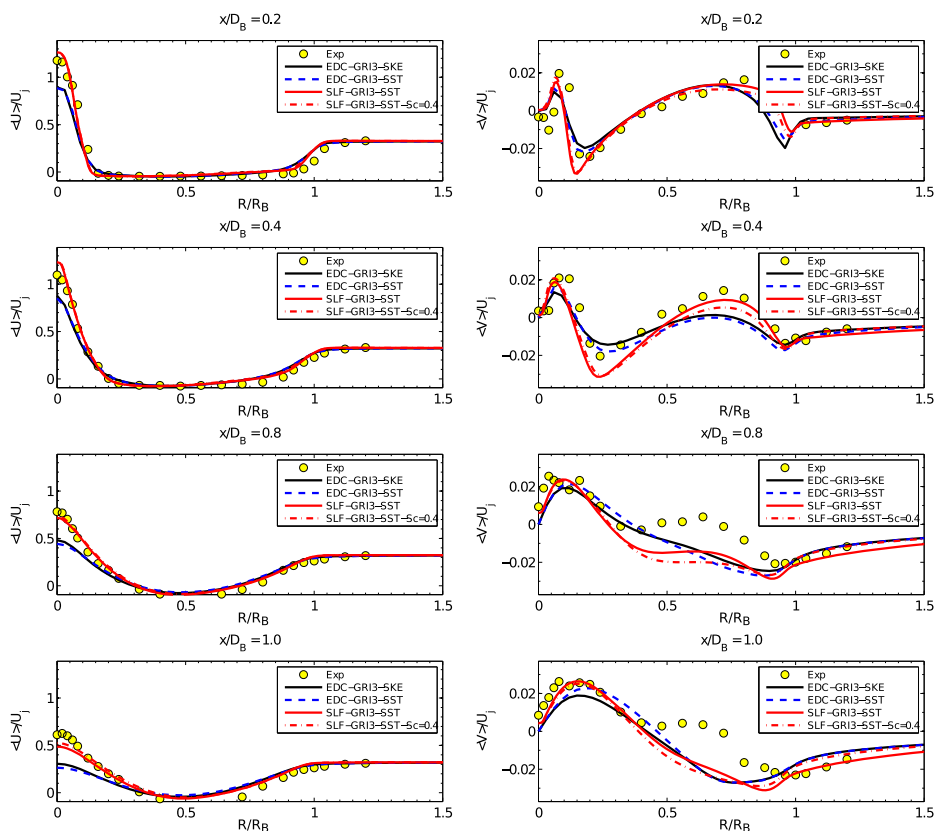


**Fig. 10** Radial profiles of the mean axial and radial velocities at different axial positions for the Sydney flame HM1E

As expected the deviations between OF runs with SKE and SST for the velocity field within the recirculation zone were not significant. The manner of implementation of the SST model in OF (via wall functions) was the main reason here. In general, the agreement between the measured data and AF with the low-Reynolds-number SST model was more accurate compared to the OF runs.

The predicted streamline pattern is shown in Fig. 11. The flame was stabilized by the recirculation zone behind the bluff-body which traps hot gases. By definition, the recirculation length ( $\langle L_r \rangle$ ) corresponds to the distance between the base of the bluff-body and the sign change of the centerline mean axial velocity. The calculated recirculation zone length was in a range of  $1.19 - 1.22 D_B$  which was consistent with the predictions by Yan et al. [59]. Precise experimental data for  $\langle L_r \rangle$  were not available, however its value could be bounded between  $X/D = 1.4$  and  $X/D = 1.8$ . Hence,  $\langle L_r \rangle$  was under-predicted in the present calculations.

Iso-contours of mean temperature and  $\langle Y_{OH} \rangle$  inside the recirculation zone are displayed in Fig. 12. Figures 13 and 14 compare time-averaged scalar fields at two axial locations inside the recirculation zone. A comparison of the predicted and measured mean temperature and other species outside the recirculation zone is displayed in Fig. 15.

In general, temperature profiles predicted by OF with the EDC-based approach matched the experimental data well. The peak in the predicted temperature profiles in the shear layer between the co-flow and the hot combustion products at  $X/D_B = 0.6$  may be explained by the artificial boundary condition for the temperature set at the bluff-body walls. The fixed constant temperature was applied at the outer surface of the bluff-body ( $T = 953$  K), which appears to lead to an inaccurate estimate of the heat transfer and consequently an over-prediction (approximately 200 K) of the temperature in the shear layer. Another feature that can contribute was the unburned fuel recirculated by the outer reversed zone which can partly burn when mixed with the fresh air, leading to some temperature increase. Figures 13–14 show that there was more  $H_2$  and CO than in the experiment at the locations of the negative axial velocity. Other possible reasons such as insufficient boundary layer and shear layer

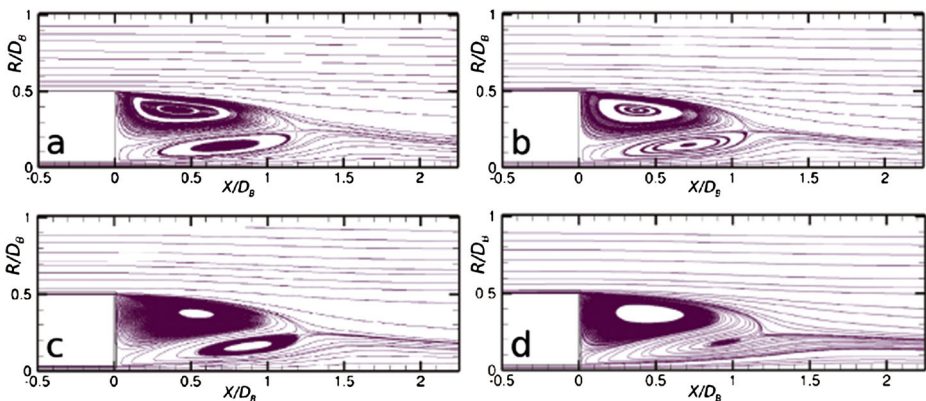


**Fig. 11** Time-averaged streamlines for the Sydney flame HM1E:EDC-GRI3-SKE (a), EDC-GRI3-SST (b), SLF-GRI3-SST (c) and  $SLF - GRI3 - SST - S_{c_i}=0 : 4$  (d)

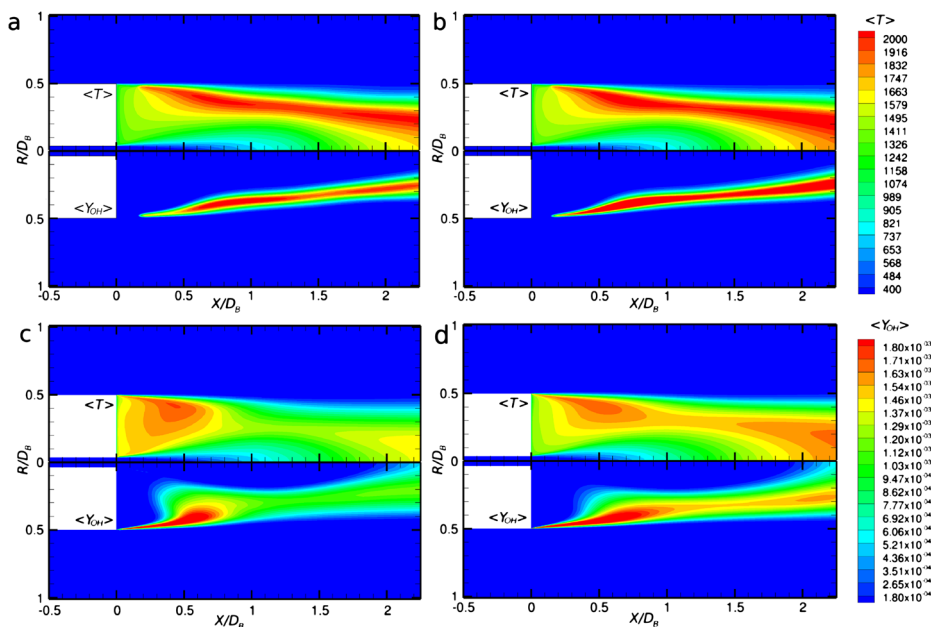


**Fig. 12** Iso-contours of mean temperature and OH mass fractions for the Sydney flame HM1E: *EDC – GR13 – SKE* (a), *EDC – GR13 – SST* (b), *SLF – GR13 – SST* (c) and *SLF – GR13 – SST –  $Sc_t = 0:4$*  (d)

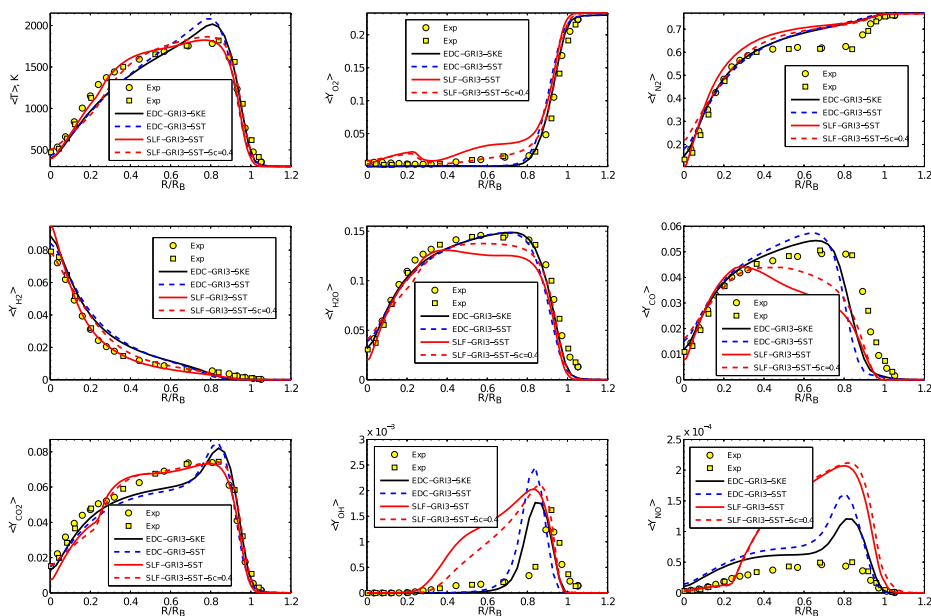


**Fig. 13** Radial profiles of mean temperature and mean composition at  $X/D_B = 0.6$  for the Sydney flame HM1E. Experiments [9] are for both sides of the symmetry axis

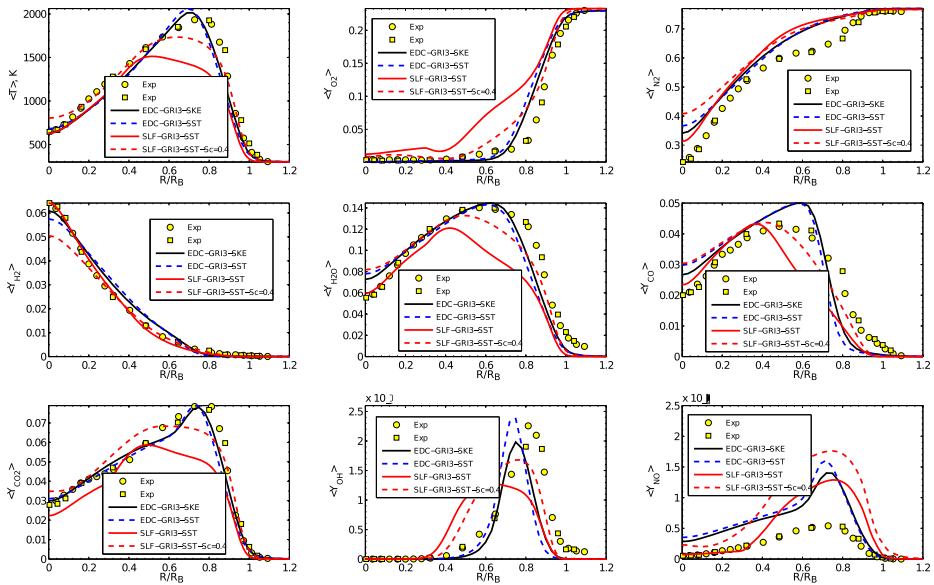


**Fig. 14** Radial profiles of mean temperature and mean composition at  $X/D_B = 0.9$  for the Sydney flame HM1E. Experiments [9] are for both sides of the symmetry axis

resolutions and the simple treatment of radiation heat transfer should be considered as well.

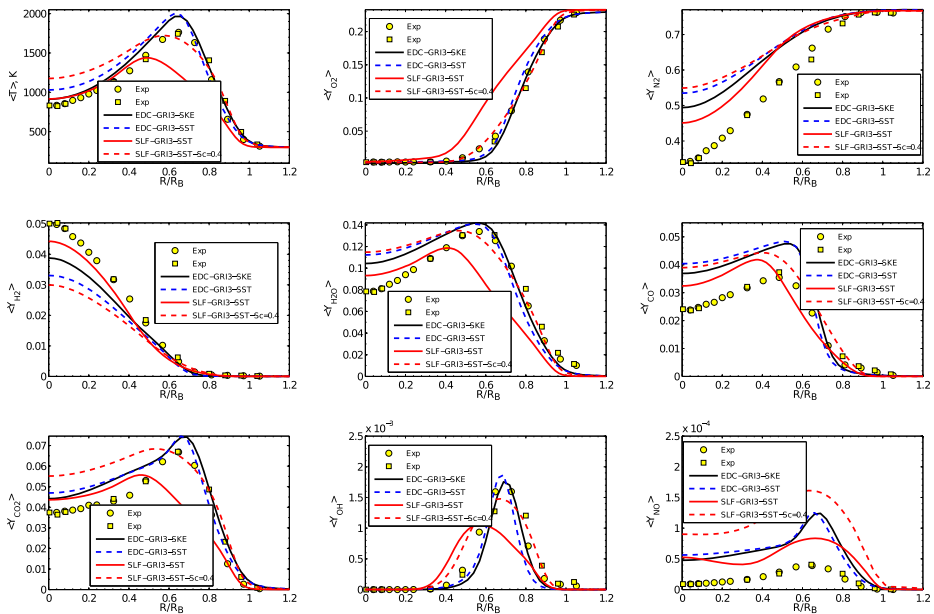


**Fig. 15** Radial profiles of mean temperature and mean composition at  $X/D_B = 1.3$  for the Sydney flame HM1E. Experiments [9] are for both sides of the symmetry axis

Further downstream a good match between results calculated by OF with the EDC-based approach and measured data for the temperature was observed. The radial profiles of  $\langle Y_{O_2} \rangle$ ,  $\langle Y_{N_2} \rangle$ ,  $\langle Y_{H_2} \rangle$ ,  $\langle Y_{CO_2} \rangle$  and  $\langle Y_{H_2O} \rangle$  matched the experimental data well. The profiles of  $\langle Y_{CO} \rangle$  were slightly over-predicted. These discrepancies could be explained by the temperature behavior in the shear layer. Prediction of OH in any combustion simulation is particularly challenging due to the strong nonlinearity of the species evolution [49]. The agreement for  $\langle Y_{OH} \rangle$  was very satisfactory which could indicate that the combustion process was represented correctly. The reaction took place in the mixing shear layer between the co-flow stream and the recirculation zone. The profiles of  $\langle Y_{NO} \rangle$  was over-predicted significantly showing only the correct trends. The production of NO is highly dependent on temperature. Thus, one of the possible reasons for such discrepancies may be an incorrect treatment of radiation which can have a dramatic effect on the predicted NO levels [13].

The match between the predicted results by AF with the SLF model was less accurate. The SLF model failed to capture peak temperature at  $X/D_B = 0.9$ . At  $X/D_B = 1.3$  the SLF model failed to represent the experimental profile. However, these results were consistent with the published data by Yan et al. [59] who used the SLF model as well. The radial profiles of  $\langle Y_{O_2} \rangle$ ,  $\langle Y_{N_2} \rangle$ ,  $\langle Y_{H_2} \rangle$ ,  $\langle Y_{CO_2} \rangle$  and  $\langle Y_{H_2O} \rangle$  had the similar trend to those of mean temperature. OH and NO were not well reproduced by AF with the SLF model as well.

Figure 16 displays profiles of conditional mean for temperature, which probably could provide a more quantitative test than scatter plots [41]. The temperature profiles matched well at  $X/D_B = 0.6$  location. Further downstream the calculated profiles of temperature failed to reproduce the peak values and in general are significantly lower than the experimental data. The calculated mixture fraction reached too lean values as well.

In the recirculation zone, with strong radial gradients of mean velocity and mean mixture fraction, it was observed a lack of turbulent diffusion. This finding was in contrast to the fact that the velocity field within the recirculation region was predicted quite accurately. Thus, there was some degree of freedom of playing with the PDF turbulence Schmidt number (here,  $Sc_t = 0.85$ ) to improve the results [42]. With this goal, another run with AF and the SLF model was conducted where the PDF Schmidt number was set to  $Sc_t = 0.4$ . The predicted results revealed a minimum impact on the flow field, except the small deviations in the distributions of the radial velocity (Fig. 10) and as a consequence on the streamline pattern (Fig. 11). Meanwhile, the predicted mean composition was improved significantly within the recirculation zone. However, the peak temperature at  $X/D_B = 0.9$  was not

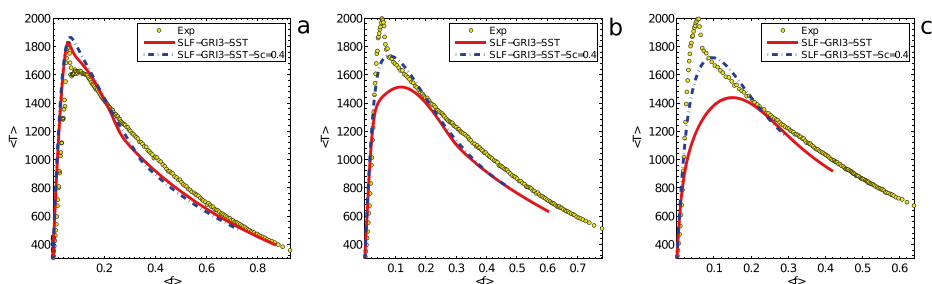


**Fig. 16** Conditional temperature profiles for the Sydney flame HM1E at three axial locations  $X/D_B = 0.6$  (a),  $X/D_B = 0.9$  (b) and  $X/D_B = 1.3$  (c)

captured well. Moreover, the large deviations were observed between the predicted and the experimental temperatures at the central axis at  $X/D_B = 0.9$  and  $X/D_B = 1.3$ . In general, OH was calculated more accurately compared to the case with  $Sc_t = 0.85$ . The profiles of NO were over-predicted as well and, in general, were less accurate than for the case with  $Sc_t = 0.85$ .

## 6 Discussion

Numerical predictions of the Sandia Flame CHNa and the Sydney Flame HM1E have been carried out. In general, in spite of some discrepancies, good agreement was achieved for both flames in terms of velocity fields, temperature and the species concentrations.

The disagreement between experimental data and numerical results is determined by two groups of errors (apart from experimental errors): (1) model errors due to inadequate assumptions made in selecting one sub-model or another (for turbulence, radiation and turbulence-chemistry interaction) and (2) discretization errors caused by the inadequate resolution of the employed computational grids and computational methods. Whereas the errors of the first group are assumed to be systematic under certain assumptions, e.g. for a fixed computational methodology, discretization errors are controlled by the method of adaptation (increase in the resolution) of a computational grid.

### 6.1 Influence of modeling errors

From the model error point of view the following critical remark should be done. Here, the turbulence-chemistry interaction was modeled using the EDC model with detailed chemistry, while the standard  $k-\epsilon$  model and the P1-approximation model were used for the turbulence and radiation, respectively. Choosing appropriate models for turbulence, chemistry and radiation would play an important role for modeling of the turbulent reacting flows.

In the present study, the influence of the radiation heat transfer was investigated for the Sandia Flame CHNa using the EDC with the GRI3.0 chemistry. The predicted difference between peak temperatures was about 140 K. However, the results showed that discrepancies between major species were insignificant. Another aspect of radiation influence on temperature prediction is an accurate estimation of NO. The present calculations were not able to predict accurately the concentration of NO for both test cases. Thus, an application of alternative radiation sub-models could be of interest in future work.

The specially designed kinetic mechanism FFR [14] was applied to simulate syngas combustion of the Sandia Flame CHNa, which demonstrated satisfactory results compared to the experimental results. To check the influence of the chemical kinetics, the Sandia Flame CHNa was calculated using EDC with the full GRI3.0 mechanism [4], which revealed only minor differences for the major species and the temperature compared to the results with the FFR mechanism. This observation correlates well with the previous results by Lilleberg et al. [29] and Zahirovi et al. [61]. The Sydney flame HM1E was predicted using only the GRI3.0 scheme due to resource limitations. Moreover, it turned out that this flame was more computationally stiff (expensive) with respect to other chemistry, compared to the Sandia Flame CHNa.

The SLF model was applied to analyze the influence of turbulence-chemistry interaction sub-modeling. For the Sandia flame CHNa the agreement between the EDC-based approach, the SLF model and the measured data was reasonable. The results obtained by the



PDF-based approaches revealed an upstream shift of the peak temperature and a more rapid decay of the jet. Such discrepancies could possibly be explained by the incompressible flow nature of the PDF-based models with the related effect of the dilatation flow, which was investigated in detail by Hewson and Kerstein [20]. The EDC-based calculations showed the correct peak temperature location, but over-predicted the peak values approximately by 240 K and could be explained by the applied turbulence model.

For the Sydney flame HM1E, the EDC-based approach revealed more accurate results compared to the SLF model. It was found that such strong discrepancies between the measured data and the results by the SLF model are strongly related to the lack of turbulence mixing due to the fixed PDF Schmidt number. Another run with the modified PDF Schmidt number  $Sc_t = 0.4$  indicated that the influence on the flow field was minor, while the composition was changed significantly but still not sufficient to match the experimental temperature at  $X/D_B = 0.9$  and  $X/D_B = 1.3$  well.

In the present study transport properties were simplified while using AF with the PDF-based approaches by neglecting the Dufour and Soret effect by introducing a single diffusion coefficient (i.e. the assumption of unity Lewis number) which may lead to considerable errors [43, 46]. Pitsch [46] provided a comprehensive analysis of the adequateness of the unity Lewis number assumption for the same type of hydrogen fueled flames where it was shown that turbulence diffusion dominates both energy and mass diffusion (even for the hydrogen radical, which has the highest molecular diffusivity, the turbulent diffusivity became larger within the first few nozzle diameters). Another remark related to the PDF-based models is the assumption of statistical independence between the mixture fraction and the scalar dissipation which remains questionable and probably was not be accurate in turbulent mixing layers [43].

With respect to the turbulence modeling the following observations were found. The EDC-based approach with the standard  $k-\epsilon$  model provided satisfactory results for the Sandia flame CHNa and the Sydney flame HM1E flame. The SLF model provided most accurate predictions of the Sandia flame CHNa when the constant  $C_{\epsilon 1}$  was set to  $C_{\epsilon 1} = 1.52$ . A change of the model constant  $C_{\epsilon 1}$  value is a common remedy to reduce spreading/diffusion and increase the predictive capabilities of the model (e.g. [29]). However, as it was discussed in Section 5.2, the conventional modified value of  $C_{\epsilon 1} = 1.6$  significantly over-predicted the flame temperature in the post-flame zone [8, 36] for the Sandia flame CHNa. Here it was found that the alternative value of  $C_{\epsilon 1} = 1.52$  may be a compromise choice to simulate the Sandia flame CHNa using the PDF-based models.

For the Sydney flame HM1E, the SLF model with the low-Reynolds-number  $k-\omega$  SST turbulence model predicted the flow field quite accurately inside the recirculation region, meanwhile temperature and the composition were predicted unsatisfactory. Furthermore, the Sydney flame HM1E was calculated using OF with the EDC-based approach coupled with the standard  $k-\epsilon$  and the  $k-\omega$  SST turbulence models and it was found that the discrepancies between these two cases were minor.

Another important aspect of combustion modeling is the radiative heat transfer. In the present study it was treated in a simple way using the P-1 approximation [6], assuming that a flame is optically thin. Sometimes, the optically thin radiation sub-model could not accurately predict the radiant fraction [13]. Thus, it will be interesting in future work to investigate these flames with a more sophisticated radiation sub-model (like a Discrete Ordinate model [48]). It is worth noticing that unphysical results were obtained using the Discrete Ordinate model for temperature at the center axis for axi-symmetrical test problems in the present study. These results were confirmed for both OpenFOAM and ANSYS FLUENT. Thus, full three-dimensional

simulations are required in order to get accurate predictions with the Discrete Ordinate model.

Furthermore, the finite-rate chemical kinetics were taken into account by treating the fine structures as constant pressure and adiabatic homogeneous reactors calculated using the Perfectly Stirred Reactor model [17]. Here the effect of radiation losses in the PSRs was neglected and more accurate formulation should be formulated and investigated in future work.

## 6.2 Influence of discretization errors

From the discretization error point of view, two sets of grids were used in the present study to check the mesh-error influence. It is worth noticing that in spite of the fact that the calculations were carried out in two dimensions, approximately 3 – 5 weeks were required to get statistically-converged solutions on the high-resolution grids using one node (16 cores in parallel) on the Vilje high-performance computing facility ([www.notur.no](http://www.notur.no)). The main reason for this was the finite-rate chemistry. This showed that turbulent reacting flow simulations with detailed chemistry are resource expensive even for two-dimensional problems. The present EDC-based calculations did not reveal significant deviations between the solutions obtained on the low-resolution (not presented here) and the high-resolution grids (except for the intermediate species, such as OH and NO). Thus, due to resource limitations, the resolution of the applied grids was concluded to be sufficient for the scope of the present work.

The influence of the temporal discretization errors was not analyzed in the present study. Usually the spatial discretization error effect is larger than the error arising from the time integration [16]. It could be shown that in case of fully developed turbulent flows, existing small time and space scales are simply advected by the most energetic eddies [16]. This argument yields an accuracy time-scale similar to the CourantFriedrichsLewy (CFL) criterion. Thus, in all present calculations, the stability condition  $CFL < 0.4$  was employed, which guaranteed that the actual time step was close to the accuracy time step.

Another important parameter is the error tolerance for chemistry system integration. This parameter influences the accuracy of the species predictions and the total computational time for each time step (iteration) as well. In the present study the absolute tolerance was set to  $10^{-5}$  and no sensitivity study was carried out. However, for the further method development it will be required to assess the influence of this parameter on the flow predictions both in terms of accuracy and computational efficiency.

## 7 Concluding Remarks

The Eddy Dissipation Concept with the detailed chemistry approach and the standard  $k-\epsilon$  turbulence model (with the standard constants) were applied to simulate the Sandia flame CHNa and the Sydney flame HM1E. The finite-rate chemistry effects were described by the FFR and the GRI3.0 mechanisms. The robust implicit Runge-Kutta method (RADAU5) was used for integrating stiff ordinary-differential equations to compute the reaction rates. The radiation heat transfer was treated with the simple P-1 model. Statistically stationary results were obtained and compared in detail with the available experimental data. In general, there was good agreement between the present simulations and measurements for both flames. It is believed that one of the main reasons for the observed discrepancies between the EDC-based predictions and experimental data for the Sandia flame CHNa was the round-jet

anomaly of the  $k$ - $\epsilon$  turbulence model. The Sydney flame HM1E was calculated with the  $k$ - $\omega$  SST turbulence model as well. However, the predicted results did not reveal any significant deviations between the standard  $k$ - $\epsilon$  model and the SST model which could be explained by the SST model implementation in OpenFOAM.

The steady laminar flamelet model was applied to investigate the influence of the turbulence-chemistry interaction. For this purpose the commercial code ANSYS FLUENT was utilized. It is worth noticing that the same grids were used and quite similar numerical methods, boundary conditions and sub-models for the turbulence and radiative heat transfer were chosen. The finite-rate chemistry effects were taken into account using the FFR and GRI3.0 mechanisms. It was found that the most accurate SLF-based predictions for the Sandia flame CHNa was obtained with the modified constant  $C_{\epsilon 1} = 1.52$ . The present results obtained with the SLF-based approach and the default value of the PDF turbulence Schmidt number  $Sc_t = 0.85$  were found to be less accurate than the EDC-based for the Sydney flame HM1E due to the lack of the turbulence mixing. The calculation with the modified Schmidt number  $Sc_t = 0.4$  showed some improvement in the prediction of the composition and temperature but was not sufficient to match the experimental data well.

Overall, the present results give a good indication on the adequacy and accuracy of the implemented solver in the OpenFOAM toolbox and its readiness for further combustion application development.

**Acknowledgements** This work was conducted as a part of the CenBio Center for environmentally-friendly energy. We are grateful to the Norwegian Meta center for Computational Science (NOTUR) for providing the uninterrupted HPC computational resources and useful technical support.

## References

1. ANSYS FLUENT R12: Theory guide. Tech. rep. (2009). Ansys Inc.
2. Barlow, R.S., Frank, J.H.: Effects of turbulence on species mass fractions in methane/air jet flames. *Proc. Combust. Inst.* **27**, 1087–1095 (1998)
3. Barlow, R.S., Fiechtner, G.J., Carter, C.D., Chen, J.-Y.: Experiments on the scalar structure of turbulent CO/H<sub>2</sub>/N<sub>2</sub> jet flames. *Combust. Flame* **120**, 549–569 (2000)
4. Bowman, C.T., Hanson, R.K., Davidson, D.F., Gardiner, W.C., Lissianski, V., Smith, G.P., Golden, D.M., Frenklach, M., Goldenberg, M.: GRI-Mech (2008). Accessed February 2013. <http://www.me.berkeley.edu/gri-mech/>
5. Chase, M.: NIST-JANAF Thermochemical tables. *J. Phys. Chem. Ref. Data, Monogr. Suppl.* (1998)
6. Cheng, P.: Dynamics of a radiating gas with application to flow over a wavy wall. *AIAA J.* **4**, 238–245 (1966)
7. Chomiak, J., Karlsson, A.: Flame liftoff in diesel sprays. In: *Proceedings of 26th International Symposium on Combustion*, pp. 2557–2564 (1996)
8. Cuoci, A., Frassoldati, A., Ferraris, G., Buzzi, Faravelli, T., Ranzi, E.: The ignition, combustion and flame structure of carbon monoxide/hydrogen mixtures. Note 2: Fluid dynamics and kinetic aspects of syngas combustion. *Int. J. Hydrog. Energy* **32**, 3486–3500 (2007)
9. Dally, B.B., Masri, A.R., Barlow, R.S., Fiechtner, G.J.: Instantaneous and mean compositional structure of bluff-body stabilised nonpremixed flames. *Combust. Flame* **114**, 119–148 (1998)
10. Dunn, M.J., Masri, A.R., Bilger, R.W.: A new piloted premixed jet burner to study strong finite-rate chemistry effects. *Combust. Flame* **151**, 46–60 (2007)
11. Dunn, M.J., Masri, A.R., Bilger, R.W., Barlow, R.S., Wang, G.H.: The compositional structure of highly turbulent piloted premixed flames issuing into a hot coflow. *Proc. Combust. Inst.* **32**, 1779–1786 (2009)
12. Fox, R.O.: *Computational models for turbulent reacting flows*. Cambridge University Press, Cambridge (2003)
13. Frank, J.H., Barlow, R.S., Lundquist, C.: Radiation and nitric oxide formation in turbulent non-premixed jet flames. *Proc. Comb. Inst.* **28**, 447–454 (2000)

14. Frassoldati, A., Faravelli, T., Ranzi, E.: The ignition, combustion and flame structure of carbon monoxide/hydrogen mixtures. Note 1: Detailed kinetic modeling of syngas combustion also in presence of nitrogen compounds. *Int. J. Hydrog. Energy* **32**, 3471–3485 (2007)
15. Ertesvåg, I.S., Magnussen, B.F.: The eddy dissipation turbulence energy cascade model. *Combust. Sci. Technol.* **159**, 213–235 (2000)
16. Geurts, B.: Elements of direct and large-eddy simulation. R.T. Edwards, Philadelphia (2004)
17. Gran, I.R., Magnussen, B.F.: A numerical study of a bluff-body stabilized diffusion flame. Part 2. Influence of combustion modeling and finite-rate chemistry. *Combust. Sci. Technol.* **119**, 191–217 (1996)
18. Hairer, E., Wanner, G.: Solving ordinary differential equations II: Stiff and differential-algebraic problems, 2nd ed. Springer Series in Computational Mathematics. Springer-Verlag (1996)
19. Hestens, M., Steifel, E.: Methods of conjugate gradients for solving systems of algebraic equations. *J. Res. Nat. Bur. Stand* **29**, 409–436 (1952)
20. Hewson, J.C., Kerstein, A.R.: Stochastic simulation of transport and chemical kinetics in turbulent CO/H<sub>2</sub>/N<sub>2</sub> flames. *Combust. Theory Model.* **5**, 669–897 (2001)
21. Hossain, M., Jones, J.C., Malalasekera, W.: Modelling of a bluff-Body nonpremixed flame using a coupled radiation/flamelet combustion model. *Flow Turbul. Combust.* **67**, 217–234 (2001)
22. Hottel, H.C., Sarofim, A.F.: Radiative Transfer.: McGraw-Hill, New York (1967)
23. Hutchinson, B., Raithby, G.: A multigrid method based on the additive correction strategy. *J. Numer. Heat Transfer* **9**, 37–511 (1986)
24. Issa, R.: Solution of the implicitly discretized fluid flow equations by operator splitting. *J. Comput. Phys.* **62**, 40–65 (1986)
25. Jones, W.P., Whitelaw, J.H.: Calculation methods for reacting turbulent flows: a review, *Combust. Flame* **48**, 1–26 (1982)
26. Launder, B., Sharma, B.: Application of the energy-dissipation model of turbulence to the calculation of flow near a spinning disc. *Lett. Heat Mass Tran.* **1**, 131–138 (1974)
27. Launder, B.E., Spalding, D.B.: The numerical computation of turbulent flows. *Comput. Method Appl. M.* **3**, 269–289 (1974)
28. Leonard, B.P., Mokhtari, S.: ULTRA-SHARP Nonoscillatory convection schemes for high-speed steady multidimensional flow, NASA TM 1-2568 (ICOMP-90-12) NASA Lewis Research Center (1990)
29. Lilleberg, B., Christ, D., Ertesvåg, I.S., Rian, K.E., Kneer, R.: Numerical simulation with an extinction database for use with the Eddy Dissipation Concept for turbulent combustion. *Flow Turbul. Combust.* **91**, 319–346 (2013)
30. Liu, K., Pope, S.B., Caughey, D.A.: Calculations of bluff-body stabilized flames using a joint probability density function model with detailed chemistry. *Combust. Flame* **141**, 89–117 (2005)
31. Lysenko, D.A., Ertesvåg, I.S., Rian K.E.: Modeling of turbulent separated flows using OpenFOAM. *Comput. Fluids* **80**, 408–422 (2013)
32. Magnussen, B.F., Hjertager, B.H.: On mathematical modeling of turbulent combustion with special emphasis on soot formation and combustion. *Proc. Combust. Inst.* **16**, 719–729 (1976)
33. Magnussen, B.F.: Modeling of NO<sub>x</sub> and soot formation by the Eddy Dissipation Concept. Int.Flame Research Foundation, 1st topic Oriented Technical Meeting., 17-19 Oct., Amsterdam, Holland (1989)
34. Magnussen, B.F.: The Eddy Dissipation Concept a bridge between science and technology, ECCOMAS Thermal Conference on Computational Combustion, Lisbon, Portugal, 21-24 June (2005)
35. Marshak, R.E.: Note on the spherical harmonics method as applied to the Milne problem for a sphere. *Phys. Rev.* **71**, 443–446 (1947)
36. Marzouk, O.A., Huckaby, E.D.: A comparative study of eight finite-rate chemistry kinetics for CO/H<sub>2</sub> combustion. *Eng. App. Comput. Fluid Mech.* **4**, 331–356 (2010)
37. Meijerink, J.A., Van der Vorst, H.A.: An iterative solution method for linear systems of which the coefficient matrix is a symmetric M-matrix. *Math. Comp.* **31**, 148–162 (1977)
38. McGuirk, J.J., Rodi, W. In: Durst, F., Launder, B.E., Schmidt, F.W., Whitelaw, J.H. (eds.): The calculation of three-dimensional turbulent free jets. In turbulent Shear Flows I: Selected papers from the First International Symposium on Turbulent Shear Flows, pp. 71–83. Springer-Verlag, Germany (1979)
39. Menter, F.R.: Two-equation eddy-viscosity turbulence models for engineering applications. *AIAA J.* **32**, 1598–1605 (1994)
40. Menter, F., Esch, T.: Elements of industrial heat transfer prediction, 16th Brazilian Congress of Mechanical Engineering (COBEM) (2001)
41. Merci, B., Naud, B., Roekaerts, D.: Impact of turbulent flow and mean mixture fraction results on mixing model behavior in transported scalar PDF simulations of turbulent non-premixed bluff body flames. *Flow Turbul. Combust.* **79**, 41–53 (2007)

42. Merci, B., Naud, B., Roekaerts, D., Maas, U.: Joint scalar versus joint velocity-scalar PDF simulations of bluff-body stabilized flames with REDIM. *Flow Turbul. Combust.* **82**, 185–209 (2009)
43. Peters, N.: Laminar diffusion flamelet models in non premixed combustion. *Prog. Energy Combust. Sci.* **10**, 319–339 (1984)
44. Peters, N.: *Turbulent Combustion*. Cambridge University Press, Cambridge (2000)
45. Pitsch, H., Peters, N.: A consistent flamelet formulation for non-premixed combustion considering differential diffusion effects. *Comb. Flame* **114**, 26–40 (1998)
46. Pitsch, H.: Unsteady flamelet modeling of differential diffusion in turbulent jet diffusion flames. *Combust. Flame* **123**, 358–374 (2000)
47. Pope, S.B.: An explanation of the turbulent round-jet/plane-jet anomaly. *AIAA J.* **16**, 279–281 (1978)
48. Raithby, G.D., Chui, E.H.: A finite-volume method for predicting a radiant heat transfer in enclosures with participating media. *J. Heat Transfer* **122**, 415–423 (1990)
49. Raman, V., Pitsch, H., Fox, R.O.: Hybrid large-eddy simulation/Lagrangian filtered-density-function approach for simulating turbulent combustion. *J. Comb. Flame* **143**, 56–78 (2005)
50. Richardson, L.F.: *Weather prediction by numerical process*. Cambridge University Press, Cambridge (1922)
51. Rhie, C., Chow, W.: Numerical study of the turbulent flow past an airfoil with trailing edge separation. *AIAA J.* **21**, 32–1525 (1983)
52. Sabelnikov, V., Fureby, C.: LES combustion modeling for high Re flames using a multi-phase analogy. *Combust. Flame*, 160, pp. 83–96 (2013)
53. Shih, T.-H., Liou, W., Shabbir, A., Yang, Z., Zhu, J.: A new  $k$ - $\epsilon$  eddy-viscosity model for high Reynolds number turbulent flows model development and validation. *Comput. Fluids* **24**, 22738 (1995)
54. Smith, T.F., Shen, Z.F., Friedman, J.N.: Evaluation of coefficients for the weighted sum of gray gases model. *J. Heat Trans-T. ASME* **104**, 602–608 (1982)
55. Warnatz, J., Maas, U., Dibble, R.W.: *Combustion*, 4th ed. Springer. Berlin Heidelberg, New York (2006)
56. Waterson, N.P., Deconinck, H.: Design principles for bounded higher-order convection schemes – a unified approach. *J. Comput. Phys.* **224**, 182–207 (2007)
57. Weller, H.G., Tabor, G., Jasak, H., Fureby, C.: A tensorial approach to computational continuum mechanics using object-oriented techniques. *J. Comp. Phys.* **12**, 620–631 (1998)
58. Williams, F.A.: *Turbulent mixing in non-reactive and reactive flows* (S.N.B. Muurthy, ed.), p. 189, Plenum (1975)
59. Yan, J., Thiele, F., Buffat, M.: A turbulence model sensitivity study for CH<sub>4</sub>/H<sub>2</sub> bluff-body stabilized flames. *Flow Turb. Combust.* **73**, 1–24 (2004)
60. Vandoormaal, J.P., Raithby, G.D.: Enhancements of the SIMPLE method for predicting incompressible fluid flows. *Numer. Heat Transfer* **7**, 147–163 (1984)
61. Zahirovic, S., Scharler, R., Kilpinen, P., Obernberger, I.: Validation of flow simulation and gas combustion sub-models for the CFD-based prediction of NO<sub>x</sub> formation in biomass grate furnaces. *Combust. Theory Model.* **15**, 61–87 (2011)